

Multifidelity validation of digital surrogates using variable-density turbulent mixing models

Benjamin Musci ^{*}*Georgia Institute of Technology, Atlanta, Georgia 30332, USA*Britton Olson [†]*Lawrence Livermore National Laboratory, Livermore, California 94550, USA*Samuel Petter [‡], Gokul Pathikonda [‡], and Devesh Ranjan [§]*Georgia Institute of Technology, Atlanta, Georgia 30332, USA*

(Received 3 March 2022; accepted 4 November 2022; published 3 January 2023)

In this study, ensembles of experimental data are presented and utilized to compare and validate two models used in the simulation of variable-density (Atwood = 0.22), compressible turbulent mixing. Though models of this kind (Reynolds averaged Navier-Stokes and large-eddy simulations) have been validated extensively with more canonical flows in previous studies, the present approach offers novelty in the complexity of the geometry, the ensemble-based validation, and the uniformity of the computational framework on which the models are tested. Moreover, all experimental and computational tasks were completed by the authors which has led to a tightly coupled experimental configuration with its “digital twin.” The experimental divergent-shock-tube facility and its data acquisition methods are described and replicated in simulation space. A 2D Euler model which neglects the turbulent mixing at the interface is optimized to experimental data using a Gaussian process. This model then serves as the basis for both the 2D RANS and 3D LES studies that make comparisons to the mixing-layer data from the experiment. A relatively simple RANS model is shown to produce good agreement with experimental data only at late flow development times. The LES ensembles generally show good agreement with experimental data but display sensitivity to the characterization of initial conditions. Resolution-dependent behavior is also observed for certain higher-order statistics of interest. Overall, the LES model successfully captures the effects of divergent geometry, compressibility, and combined nonlinear instabilities inherent to the problem. The successful prediction of mixing width and its growth rate highlight the existence of three distinct regimes in the development of the instability, each with similarities to previously studied instabilities.

DOI: [10.1103/PhysRevFluids.8.014501](https://doi.org/10.1103/PhysRevFluids.8.014501)

I. INTRODUCTION

The mixing of variable-density flows occurs across a vast range of space and timescales. It occurs on Astrophysical scales in events like supernovae (SN), on kilometer scales in oceanic

^{*}Also at Lawrence Livermore National Laboratory; bmusci3@gatech.edu

[†]olson45@llnl.gov

[‡]Also at Arizona State University.

[§]devesh.ranjan@me.gatech.edu

and atmospheric flows, all the way down to the millimeter scales of inertial confinement fusion (ICF). In ICF and SN, in particular, it is particularly challenging to recreate the exact mixing for scientific observation and study. This difficulty in physical observation has placed a great need for the use of computer simulations as tools for increasing understanding. However, these powerful models can in turn create more questions, and as such their efficacy requires experimental validation. For instance, a simulation used to model the multiple combined instabilities occurring in an ICF capsule should first be shown to successfully model the mixing driven by a single combined instability in a meter-scale experiment. The current work aims to achieve just that: use high-fidelity, combined-instability experimental data to create and validate a “digital-twin” simulation using two common turbulent mixing-models.

A. Problem outline and motivation

The interaction of a blast wave (BW) and a multicomponent gaseous interface results in a combined hydrodynamic instability when the BW travels from a high to low-density gas [1,2]. In this study the two gases forming the interface are N_2 and CO_2 , yielding an Atwood number (A) of 0.22. In this case, the blast-interface interaction incites the Richtmyer-Meshkov instability (RMI) at the onset followed immediately by the Rayleigh-Taylor instability (RTI) [3–9]. Any initial perturbations present on the interface create local misalignment between the density gradient and the driving, time-dependent pressure gradient, resulting in vorticity deposition on the interface due to the RMI and RTI. The vorticity deposition causes the perturbations to grow into inter-penetrating spikes (high-density gas) and bubbles (low-density gas). We refer to these combined effects as the blast-driven instability (BDI). For a comprehensive and up-to-date survey of research on the RMI and RTI, see Zhou [10,11].

Combined instabilities such as the BDI have been shown to be particularly troublesome for ICF; making their elucidation a crucial step for the viability of this technology [12–17]. Laser drive asymmetry and fabrication irregularities create perturbations that grow due to combined instability during the initial implosion stage and later on when compressed hot fuel decelerates the colder imploding fuel [15–18]. While RM growth within the capsule has been shown to have a small effect, it serves to initialize the dominant RTI growth of the implosion phase [19,20]. The instability we study is analogous: RMI acts immediately to set the stage for the longer time RTI growth.

Furthermore, it has been found that the ICF operating regime is located on a performance cliff, meaning small deviations in model design could have a large impact on performance [12]. This predicament provides impetus to rigorously test the simulations, and their models, used in ICF design as much as possible. From a more general standpoint, the simulation of compressible and turbulent environment such as the BDI pose large challenges for simulations. This is primarily because the numerical techniques utilized to capture shock discontinuities often directly impair the method’s ability to resolve turbulence in the flow [21].

B. Novelty of present work

The experimental data on their own provide three unique opportunities for model validation. Primarily, RTI and RMI have been studied extensively in the past decades, but most often in planar geometries. The models, theories, and key governing parameters (such as the self-similar growth constants), were mostly developed with planar studies. Because these models and theories have often times not been developed or validated in cylindrical or spherical geometries, they can introduce errors when used in those regimes [12]. While several recent experimental studies concerning instability growth in cylindrical geometry exists, many are concerned with the convergent case [22–24]. There are some that study the divergent case, such as Li *et al.* [25]. However to the authors knowledge, in all previous works, there is only a single instability acting, and many do not transition toward a turbulent mixed state. The present work addresses this by providing experimental data in cylindrical geometry with more complex physics (combined instability with

turbulent mixing) for comparison to simulations, RMI/RTI models, and theories. Second, the experiment provides a combined RMI/RTI instability with which to validate models. The nonlinear coupling of instabilities have previously been difficult to predict [26]. Last, the experimental data was taken using high speed (4.75–7 kHz) methods and is temporally well resolved. This allows for high-fidelity simulation validation in that the entire temporal evolution of the instability can be compared directly from experiment.

Beyond the novelty of the experimental data themselves, the simulations in this study represent a high-fidelity representation of the experimental configuration. With both simulations and experiment completed by the authors, nuances of the experimental initial conditions, boundary conditions, and the data acquisition and processing were fully replicated in the simulation. An important example of this is the characterization of interface initial conditions (ICs). Many simulations do not use real ICs to seed their simulations, while those that do often use an idealized version of an experimental IC [27]. For example, in Boureima *et al.* [28] a cosine superposition with an idealized Gaussian distribution of initial amplitudes and phases was used to seed multimodal perturbations. Experimental studies often contribute to this problem due to an outright neglect of IC characterization (sometimes due to practicality) or the diagnostic inability to measure more than a large-scale perturbation.

The use of poorly characterized ICs is particularly problematic for transitioning instabilities like the BDI, as several works have shown the imprint of ICs lasting into the late time flow properties and significantly impacting the flow evolution [11,19,27,29–37]. The ICs in this study were characterized using two different methods. One method used the energy spectra (from ≈ 300 IC realizations), and the other used direct data input of the experimental ICs. This process is covered in more detail in Sec. III E.

The present study offers novel model comparison and validation through ensembles of data. More specifically, the experimental data was used to produce mean and variance profiles for the quantities of interest. These mean profiles were used to tune the Euler and Reynolds-averaged Navier-Stokes (RANS) stages of the model validation. However for the large-eddy simulation (LES), we use the same number of LES realizations as there are experimental realizations. Then, both the mean and the variance of the LES ensemble are compared to that of the experiment. It is in this way that the study attempts to more accurately recreate the high sensitivity to ICs in this nonlinear instability.

To the authors knowledge, no previous works have used this level of ensemble-based comparison between experiment and multiple turbulent models. For instance, Barmparousis and Drikakis [38] compared ensembles of RANS and LES models to study RMI uncertainty, but did not involve experimental observations or ICs. Clark and Zhou [39] and Zhou [40] both simulated an ensemble of synthetic and artificial ICs using LES, but the studied RT flows had no link to experimental observations or RANS models. Narayanan and Samtaney [41] compared simulated RMI to experimental shock tube data, but neither the experimental data or simulation data were ensembles. Finally, over 20 years ago Dalziel *et al.* [42] performed an ensemble of RTI experiments and compared them to LES simulations from two different ICs, but the comparisons were primarily qualitative and the ensembles themselves only consisted of a few runs. Indeed, it seems extremely rare to find examples of ensemble studies for instability and mixing problems, let alone those also linked to experimental data.

Finally, the model validation occurred in an hierarchical approach. First, the initial conditions and boundary conditions are set by matching zeroth-order experimental data (such as pressure profiles) to results from the direct solution of the Euler equations, i.e., the Euler model. The Euler simulation tuning parameters are then set as constants for the mix-model simulations. A $K - L$ RANS model [43–45] is validated by tuning three model parameters to best match experimental data like interface mixed width. The second mix-model investigated is a 3D LES model, which is validated using an ensemble approach as mentioned above. All three models used in this study are implemented using the Pyranda code [46], an open source proxy-app for the Miranda code developed at Lawrence Livermore National Lab.

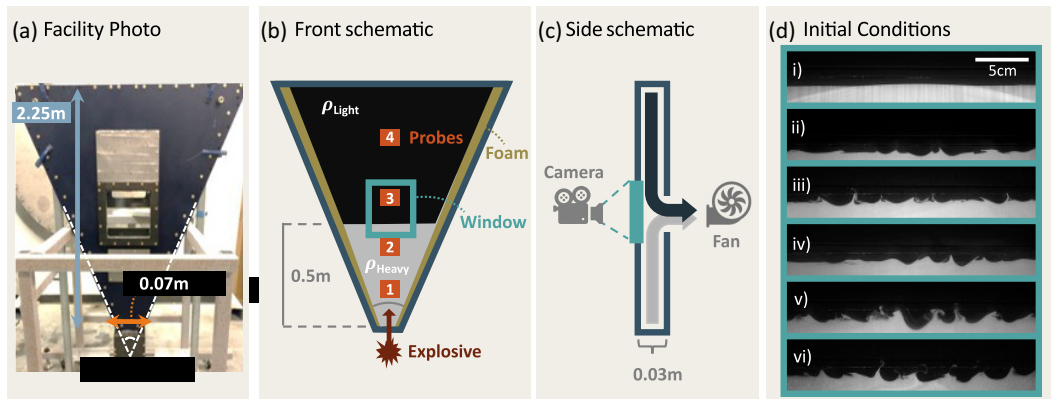


FIG. 1. Pictures and diagrams of the experimental facility. (a) Front facing picture of the diverging facility with key dimensions annotated. The viewing window can be seen in the center of the image. (b) Front facing schematic of the facility. The location of the foam layer, viewing window, and commercial detonator are all indicated. The heavy and light gas are also indicated and colored according to their appearance in Mie Scattering images. Note that for PIV, the data come from a smaller field of view located within the window indicated here. (c) Side-facing schematic of the facility showing facility width, gas entry and exit points, as well as fan and camera locations. (d) Individual initial condition realizations visualized using Mie Scattering. (i) Flat interface condition. The incident blast wave, smooth and free of perturbations, can also be seen (brightly shaded region) impacting the interface. (ii–vi) An array of perturbed initial conditions demonstrating the range of different perturbation amplitudes and wavelengths generated by the facility.

In summary, the goal of the present work is to create and demonstrate a high-fidelity numerical model of our experimental facility to test and validate RANS and LES models through comparisons of the ensemble data. The fidelity of the numerical model will be high enough for it to act as a “digital twin” and be used for future experimental design work. It should be noted, particularly concerning the RANS model, that this work does not intend to generically validate physical models. The focus is on validation of a digital surrogate in a staged multi fidelity approach, making the validation somewhat unique to this particular problem. Despite the problem specific validation, we argue there are still takeaways that can be more broadly generalized. This could in turn improve the confidence in results when using these models in much less controlled problems, such as ICF or SN. The paper is presented in the following manner. First the experimental facility and data are introduced and explained. Next the Pyranda code and the equations of motion are introduced, along with the staged-validation approach. Table I explains the differences between the models while Table II shows the coefficients used in the RANS model. The subsequent three sections cover the specific validation steps for each of the three models used (2D Euler, 2D RANS, and 3D LES) with their corresponding experimental data. The final section discusses the results of the validated simulation. Table III contains a list of the acronyms and nomenclature used in this work.

II. EXPERIMENTAL FACILITY

A. Facility and data overview

The experimental facility used to acquire the validation data has been detailed and characterized previously in Musci *et al.* [47], but will be briefly summarized here. Figure 1 shows a photo, schematics, and examples of initial conditions produced by the experimental facility. As shown in Fig. 1(a) the chamber is triangular in shape as it is intended to emulate a sector of a cylindrical disk. It consists of two 45° diverging steel plates with about 3 cm of spacing in-between. The experiments

take place in the center of this space. The chamber is over 2 m tall to allow for longer experimental times by minimizing reflected rarefaction waves from the top, which is open to the ambient.

Figures 1(b) and 1(c) show schematics that explain the operation of the facility. Two gases of different density fill the chamber—the high-density gas (ρ_{Heavy} or ρ_H), CO_2 , enters from the bottom, while the low-density gas (ρ_{Light} or ρ_L), N_2 , enters from the top. The gases exit 0.5 m above the chamber bottom through a horizontal slot due to suction created by a fan attached to the outer wall of the chamber. The fan causes slight variations in the initial gas velocity which introduces small perturbations, \mathcal{O} (mm) amplitudes, along the interface. The facility can also be operated such that the interface remains flat and unperturbed, as is shown in Fig. 1(d.i). Otherwise, Fig. 1(d.ii–vi) shows examples of perturbed initial conditions. The perturbed interface can exhibit a range of different amplitudes and wavelengths from run to run but nominally produces perturbations with initial amplitudes ranging from 1–8 mm and wavelengths between 2 and 6 cm. The impact of the outflow slot and extraction fan has been observed experimentally to have a negligible effect on the interface trajectory and development.

The facility generates blast waves using a commercial detonator (RP80 from Teledyne RISI) placed at the bottom vertex of the chamber. Upon detonation a BW travels upward, impacts the interface, and causes instantaneous hydrodynamic development. The BW has a Mach number of approximately 1.4 before interface impact. The large width to depth ratio of the facility (62 cm wide at the interface location gives a ratio of 21) helps to reduce any out-of-plane dynamics and keeps the dynamics approximately 2D (except at the fine scales, where 3D turbulence develops). Additionally, to isolate the physics of interest, a thin layer of foam is added along the facility side walls, as indicated in Fig. 1(b). This has been observed to eliminate the reflected bow shocks resulting from the BW-side wall interaction without impacting the hydrodynamic behavior at the center of the facility. It is also important to note that the cylindrical BW impacts a flat interface [Fig. 1(di)], making the setup nonaxisymmetric. This is particularly important during the mixing analysis, when the spanwise-averaging of the mixed layer is completed. While the simulation's identical geometry allows for direct comparison with these experiments, it makes comparing the results of this spanwise-averaged nonhomogeneous layer to other studies harder to interpret. It also highlights the importance of carrying out the exact same analysis procedure in the simulation, which is done here.

For all flow visualization diagnostics, the high-speed cameras used are only able to record the physics occurring in the facility's viewing window. The relative size and location of this window is indicated in Figs. 1(b) and 1(c) and can also be seen in Fig. 1(a). For the present study three types of data were used. (1) Dynamic pressure transducers and probes (DPT—model PCB 113B27) were used to record time resolved pressure traces at four locations along the length of the facility. The position of these four probes are indicated in Fig. 1(b) and allow for the tracking of the BW front. (2) High-speed Mie scattering was used to illuminate the fog seeded heavy gas and obtain large-scale mixing or interface trajectory data within the viewing window. (3) High-speed particle image velocimetry (PIV) was used to obtain 2D velocity field data for the evolution of the instability. However, to achieve adequate resolution, the PIV data was taken from a smaller field of view, located within the main and larger viewing window used for type (2).

B. Modeling challenges

1. Boundary and initial conditions

Along with exactly matching the facility's diverging geometry, there were several other unique details which had to be captured by the simulation. First was the method used to simulate the explosion of the detonator at the bottom of the chamber. While the direct simulation of the detonator could be the subject of its own research effort, the goal of this work was to simply induce the generation of a BW with characteristics that matched the experimental data. This was done in the digital twin using a small “energy pill,” the equation for which is shown in Eq. (1). A user specified quantity of total energy (E_o) is placed inside a small, pressurized sphere (containing the

local gas) which declines steeply, following a radial Gaussian profile, to the ambient at the radius (R). The motivation behind this method being that releasing a large amount of energy in such a small space, would allow the simulation to form a Taylor-Sedov BW [48,49] in the localized gas absent of any detonation mechanism or by-products. Musci *et al.* [47] has previously shown that a Taylor-Sedov BW is produced by this experimental facility. Experiments have also consistently shown the cylindrical BW to be smooth and free of perturbations prior to interface impact. The radius (R) and location of the energy pill were motivated by the actual size and location of the detonator used in the experiments:

$$E_{\text{pill}} = E_o e^{-r^2/R^2}. \quad (1)$$

The second modeling challenge is the presence of foam material along the side walls of the experimental facility. The foam which is sandwiched between the two large face plates, is placed on the diverging side walls and extends roughly two inches into the chamber. This is present to eliminate the reflected shocks that are created as the BW propagates up the chamber. It was seen experimentally that the reflected shocks impacted the hydrodynamics of the instability substantially. Thus, to isolate the effects of the incident BW-interface interaction, the foam was added and shown to eliminate all reflected waves. This was emulated in the simulation by placing a custom boundary condition along the edges of the 2D domain. It should be noted that trying to accurately model the physics of the shock-foam interaction was not the goal; it was simply desired to eliminate reflections off the side wall. This was accomplished by applying a low pass Gaussian filter (as in Cook [50]) to the flow field in the same physical location as the foam in the experiment. The velocities at the walls were set to zero, and transition between the filtered foam region and unfiltered flow region was defined using a hyperbolic tangent function with a thickness of a few computational grid points. This is all accomplished using Eqs. (2):

$$\check{w} = \frac{1}{2} \left(1 + \tanh \left\{ \frac{-[(x - x_L) - SW]}{\frac{1}{2}SW} \right\} \right) + \frac{1}{2} \left(1 + \tanh \left\{ \frac{[(x - x_R) + SW]}{\frac{1}{2}SW} \right\} \right), \quad (2a)$$

$$\vec{u} = \vec{u}(1 - \check{w}) + G_x(\vec{u})\check{w}, \quad (2b)$$

where SW is the physical thickness of the sponge and x_L and x_R are the locations of the left and right solid boundaries for a given chamber height, y . The filter weight \check{w} is then used to update the velocity equations after each substep of the fourth-order Runge-Kutta integration scheme. $G_x(\vec{u})$ is the Gaussian filter applied only in the x -direction aligned index.

Similarly, the outflow BC had to be modified to match that of the experiment. The experimental facility has an open lid, such that the BW passes through the chamber and freely into the ambient. The chamber height was made such that by the time the BW exits the chamber it has weakened substantially. The weakened BW exits the facility and sends a reflected rarefaction wave back into the chamber. The rarefaction has been observed to impact the hydrodynamics of the instability, minimally, at late times (> 11 ms). To mimic this feature in the digital twin, the outflow was formed so that minimal reflections would be created at the top boundary. This is achieved by filtering the flow as it approaches the top of the domain and enforcing ambient conditions at the boundary.

2. Losses

Unmeasured losses in the experimental facility undoubtedly affect flow field physics, and so must be accounted for in the digital twin. For instance, prior to accounting for losses the simulations displayed excessive interface movement as compared to experimental observations. The extra, late-time, movement of the interface indicated that more energy losses were occurring in reality than was being produced by simulations.

The energy losses are partially due to material and plate deflection both when the detonator explodes and as the BW traverses the chamber. Outflow losses could also occur along the length of the chamber as the BW passes things like modular port plates or viewing windows, and the high pressure forces fluid out of imperfect seals. However, a simple deflection analysis showed that the

losses from the pressurized fluid interacting with the plates was likely small compared to those due to turbulent boundary layers.

Thus, energy losses due to the formation of turbulent boundary layers along the faces of the large 45° plates were assumed to be the primary source of loss and motivated the loss-model. The boundary layers have not been experimentally measured but certainly dissipate some flow momentum into internal energy. The combination of losses acting in the system are nonlinear and cannot be easily accounted for by simply changing the input energy delivered by the detonator. To account for this in the digital twin, a drag model was used to create a loss term in the equations of motion, which then accounted for the excess energy that was being delivered to the interface in the model (which was not there in the experiment). This model will be discussed further in Sec. III B. Those wishing to skip ahead to the results and validation section should see Sec. III C.

III. MODEL DETAILS AND METHODS

The simulation tool used in this work is Pyranda—the open-source proxy app for the Miranda code developed at LLNL. Pyranda uses the same tenth-order central finite-difference scheme in space and explicit fourth-order Runge-Kutta time integration scheme as those used in Miranda. Full details of the numerical method used in Miranda are available in Cook [50]. Pyranda is a Python-based, hyperbolic PDE solver capable of solving the 3D compressible Navier-Stoke equations. For numerical discontinuities (shocks, contacts, material interfaces) we use an artificial diffusivity method similar to that of Cook [50] to regularize the solutions. The exact form of these diffusivities is given in Morgan *et al.* [51] and in Sec. III B below. While Pyranda is the base solver, or host code, used in all aspects of this work, LLNL’s RANSBox solver is used for the RANS portions of this work [45]. RANSBox is a 0-dimensional physics package with numerous RANS model capabilities ($K - \epsilon$, BHR, $K - 2L - a$, etc.) which works in tandem with the host code. RANSBox solves the RANS equations’ turbulent source-terms and diffusivities, while relying on the host code for the calculation of all spatial and temporal derivatives.

All simulations are run on a 2D (Euler and RANS) or 3D (LES) conformal structured mesh, where grid spacing is much finer near the bottom vertex of the chamber domain and gets progressively coarse in the vertical direction. The mesh is designed such that there are twice as many grid points in the vertical direction as there are in the horizontal.

A. Staged validation approach

An aspect of novelty in the current study is the approach taken for model validation. As opposed to validating a single RANS or LES mix-model against experimental results, this study validates both simultaneously. Due to this, the model validation occurs in a staged approach, whereby a nonmixing, 2D Euler validation is completed before moving on to the mix-model validation.

Figure 2 shows the staged validation approach as a schematic. The bottom of Fig. 2 shows a legend and the top shows the four types of experimental data used to assess model performance. The four experimental data types exist in two classes: nonmix and mix data. The nonmix data consists of pressure profiles obtained from the DPTs during *single*-gas runs, and interface trajectory data obtained from high speed Mie Scattering during two-gas runs with a flat IC. This nonmix data was used first to validate the 2D Euler model, which is itself a nonmixing model.

The mixing models, however, are both validated against the experimental mix data, which consists of high speed PIV data in the form of turbulent kinetic energy (TKE or k) estimations and integral mixing-width (W) data obtained from high-speed Mie Scattering. All experimental mix data was for runs with a perturbed IC. Thus, the four data just outlined are also the quantities of interest (QOI) which models will output for comparison. To summarize, the four primary QOI used for model-experiment comparison are: pressure probe data, flat interface trajectory, integral mixed width [W —Eq. (27)], and TKE [k —Eq. (28)].

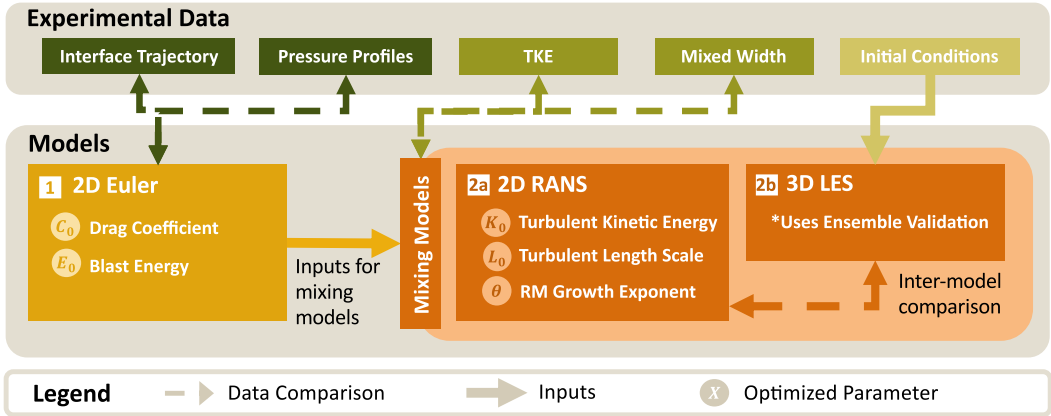


FIG. 2. A diagram outlining the staged validation approach taken in this study. (1) Stage 1 is considered the baseline solver: the 2D Euler model. The Drag Coefficient, C_0 and initial Blast Energy, E_0 , are tuned to optimize agreement with experimental data. The data used for comparison in Stage 1 are the interface trajectory and pressure profile data. Once optimized, C_0 and E_0 are set as constants and used as inputs for Stage 2. (2) Stage 2 involves validation using mixing models. (2a) Stage 2a uses a 2D RANS model where the initial turbulent kinetic energy, K_0 , initial turbulent length scale, L_0 , and self-similar RM Growth Exponent, θ are used as tuning parameters to optimize agreement with experiment data. The experimental data used for comparison in Stage 2 are TKE and interface mixed width. (2b) Stage 2b involves validation with a 3D LES model. No optimized parameters are used in Stage 2b because the 3D LES model is not tunable. Further, a data-driven representation of the experimental interface Initial Conditions are used as inputs to Stage 2b. Representative ICs for each experimental realization allow for the 3D LES model to be ensemble validated by comparing the mean and variance data against the experimental data. Finally, the model outputs of Stages 2a and 2b are compared against each other using quantities of interest not available in the experimental data set.

The tuning parameters used in each of the three computational models are shown as circles in the boxes of Fig. 2. How these parameters make their way into the model’s governing equations are shown in Sec. III B.

In the Euler model validation (Stage 1), two model parameters were used to optimize the simulation output against the nonmix experimental data. These parameters are indicated by the circles in the “2D Euler” block in Fig. 2, and are the drag coefficient, C_0 , and the initial blast energy input to the energy pill, E_0 . These parameters were varied in both single-gas and two-gas Euler simulations until they produced an optimum solution when compared to the experimental pressure and interface data. The optimum solution was determined by minimizing the error between the simulation output and the experimental data and is outlined in Sec. III C.

In Stage 2, the mixing experiments utilizes the same detonators and divergent geometry as Stage 1, C_0 and E_0 are set to constants and used as inputs to the “Mixing Models” shown in orange in Fig. 2. Comparison of the RANS and LES models is the next stage (2a and 2b) in the validation and can be performed concurrently. The mixing models are both validated against the experimental mix data, which consists of high speed PIV data in the form of TKE measurements and integral mixing width data obtained again from the high-speed Mie scattering. All experimental mix data was for 27 different runs, each with a perturbed IC.

It is important to note that the 2D Euler computational model serves as the base code for both the RANS and LES mix models. The Pyrauda framework allows for additional capabilities, degrees of freedom, transport equations and more to be integrated into the base Euler model code. This allowed us to maintain a single model and source code defining the hierarchy which has proved valuable in ensuring consistency.

TABLE I. Summary of the different spatial dimensions and terms used in the EOM for each of the validated models.

	Dim.	$\Gamma_{Y_{k,j}}$	Γ_{u_i}	$\Gamma_{\tau_{ij}}$	Γ_E	Γ_{q_i}
Euler	2	0	Eq. (15)	0	Eq. (15)	0
RANS	2	Eq. (16)	Eq. (15)	Eq. (17)	Eq. (20)	Eq. (19)
LES	3	0	Eq. (15)	0	Eq. (15)	0

As seen in the orange “RANS” box in Fig. 2, the RANS model was optimized using three model parameters: initial turbulent kinetic energy, K_o , initial turbulent length scale L_o , and the self-similar RMI growth exponent, θ . These three parameters were varied to optimize the simulation outputs against the experimental mix data, namely windowed TKE and integral mixed width. It should be emphasized that the authors were interested in evaluating RANS model performance with relatively little alterations or tuning. Thus, this work does not aim to validate the K - L RANS model with the level of rigor to improve its usage outside this particular problem.

Comparisons of the LES model to the experimental mix data did not involve determining any optimal model parameters like the previous stages, as shown in Fig. 2. The LES model, however, requires that the ICs of the interface be explicitly defined. Given the strong dependency of the mixing on the ICs, an ensemble of representative samples of the ICs were required in both the experiment and simulation to generate significant means in the data. Two approaches were taken in initializing the LES ICs. The first used a statistical model of the experimental ICs and then sampled from that model to generate the ICs for the LES. The second approach directly replicated the interface profiles of the 27 experimental runs as the LES ICs. Both approaches showed good agreement of the ensemble mean mixing width versus time. The direct data approach, however, appeared to be able to match the experimental ensemble variance far better, as will be illustrated in Sec. III E. Last, the simultaneity of validation for RANS and LES, allows for inter model comparison between the two. An LES data set that has compared favorably to the available experimental data can then be used to compare and improve RANS models where experimental data are lacking.

A final point regarding the simulation data acquisition methods should be made here. To most faithfully compare simulation outputs with experimental data, the process of data acquisition in the simulation sought to exactly mimic that in the experiment. For the nonmix pressure profile data, that meant creating simulation “probes” and placing them at the same locations as the DPTs in the experimental facility. Pressure data from these probe locations were then sampled at a rate exceeding that in the experiment. All other experimental data was captured via cameras acquiring images from the viewing window in the center of the facility. Due to this, an identically sized and located “window” was created in the simulation domain, and all data used for comparison had to be sampled from that region alone. For instance, Mie scattering data were simulated by generating images from the mass fraction field at the same resolution and domain extent as the experimental photographs. These images are then post-processed with the same scripts as experimental data. Similar routines were used for the simulation acquisition of interface trajectory data, integral mixed width, and TKE.

B. Governing equations of motion

All equations used in each of the three models are included below. The implementation of each model necessitates changes to the base equations introduced in this section. These changes, such as dimensionality or term values, will be specified in the section pertaining to that model. Of particular note are the Γ terms on the right-hand side of most equations. These terms indicate source (or sink) terms which change values depending on the model implemented and will be discussed in the respective section. These terms and their value for each respective model are shown in Table I.

The general governing equations for the mass, momentum and energy of this compressible, nonreacting, multi-component model are as follows:

$$\frac{\partial}{\partial t}(\rho Y_k) = -\frac{\partial}{\partial x_i}(\rho Y_k u_i + J_{k,i}), \quad (3)$$

$$\frac{\partial}{\partial t}(\rho u_i) = -\frac{\partial}{\partial x_j}(\rho u_j u_i - \tau_{ij}) + \rho g_i + \Gamma_{u_i}, \quad (4)$$

$$\frac{\partial E}{\partial t} = -\frac{\partial}{\partial x_i}(E u_i - \tau_{ij} u_i - q_i) + \rho g_i u_i + \Gamma_E. \quad (5)$$

Here ρ is density, Y_k is the mass fraction of species k , t is time, u_i is the velocity vector, x_i is the spatial vector, and J_k is the diffusive mass flux of species k . The diffusive mass flux of each species in Eq. (3) is given by

$$J_{k,i} = \rho D \frac{\partial Y_k}{\partial x_i} + \Gamma_{Y_{k,i}}, \quad (6)$$

where D is the molecular diffusivity, which is approximated as a scalar for species diffusion between two species. $\Gamma_{Y_{k,i}}$ is an added mass flux source and sink.

In Eqs. (4) and (5), τ_{ij} is the viscous stress tensor, g_j is the gravitational body force vector, and Γ_{u_i} is an added loss force vector which will be expanded upon below. E is total energy and Γ_E is an added energy source and sink term which will also be described below. q_i is the heat flux vector and is described by

$$q_i = \kappa \frac{\partial T}{\partial x_i} + \Gamma_{q_i}, \quad (7)$$

where κ is the thermal conductivity, T is the temperature, and Γ_{q_i} is an added heat flux term.

The form of the viscous stress tensor for a compressible fluid can be expanded upon by

$$\tau_{ij} = 2\mu S_{ij} + \left[\left(\beta - \frac{2}{3}\mu \right) \frac{\partial u_i}{\partial x_i} - p \right] \delta_{ij} + \Gamma_{\tau_{ij}}, \quad (8)$$

where μ is the dynamic and shear viscosity, S_{ij} is a symmetric tensor representing deformation of a fluid element due to the rate of strain it is subject to, δ_{ij} is the Kronecker δ , p is the static pressure, and β is the bulk viscosity. β is normally 0 for incompressible flows and also for compressible flows where the Stokes assumption holds. This assumption being that there is negligible difference between the mechanical and thermodynamic pressures, i.e., where thermodynamic equilibrium is maintained. However, during rapid expansion or compression of a fluid in situations such as the BDI, the molecular distribution of internal energy can be heavily skewed to the translational modes (as compared to the rotational and vibrational modes) and drive thermodynamic nonequilibrium, where β must be greater than 0 [52,53]. The strain rate tensor, S_{ij} , can be further expanded to

$$S_{ij} = \frac{1}{2} \left(\frac{\partial u_i}{\partial x_j} + \frac{\partial u_j}{\partial x_i} \right). \quad (9)$$

A mixed fluid equation-of-state is found using

$$\begin{aligned} \gamma &= \frac{c_{p_k} Y_k}{c_{v_k} Y_k}, & R &= R_u \frac{Y_k}{MW_k}, \\ p &= \left(E - \frac{1}{2} \rho u_i u_i \right) (\gamma - 1), \end{aligned} \quad (10a)$$

such that

$$T = \frac{p}{\rho R}. \quad (10b)$$

Here γ is the specific heat ratio, c_{p_k} and c_{v_k} are the constant pressure and volume specific heats of species k , respectively, MW_k is the molecular weight for each species, and R is the apparent gas constant of the mixed fluid with R_u as the universal gas constant.

Artificial transport terms are added to the bulk viscosity β , the dynamic viscosity μ , the thermal conductivity κ , and the molecular diffusivity D_k for each species k . Each artificial term is also Gaussian filtered in the same process as that of Morgan *et al.* [51] but is also outlined here for clarity. The fluid properties are defined as

$$\mu = \mu_f + C_\mu \overline{|\Pi(|S_{i,j}|)|} \rho, \quad (11a)$$

$$\beta = \beta_f + C_\beta \overline{\Pi\left(\frac{\partial u_i}{\partial x_i}\right)} \rho, \quad (11b)$$

$$\kappa = \kappa_f + C_\kappa \frac{\rho}{T \Delta_t} c_v G(T), \quad (11c)$$

$$D_k = D_{k,f} + \frac{\rho}{\Delta_t} \max[\Pi(Y_k)C_{D_k}, C_Y(|Y_k| - 1 + |1 - Y_k|)\Delta^2] \quad (11d)$$

$$C_i = \begin{cases} 1 \times 10^{-3}, & i = \mu, \\ 1 \times 10^{-1}, & i = \beta, \\ 1 \times 10^{-3}, & i = \kappa, \\ 1 \times 10^{-4}, & i = D_k, \\ 1 \times 10^2, & i = Y, \end{cases} \quad (11e)$$

where f denotes the physical and real contribution to the fluid transport property and all additional right-hand side terms make up the artificial contribution. For the artificial terms, the overbar indicates the application of a truncated Gaussian filter, Δ is the local mesh spacing, and Δ_t is the instantaneous time step of the solver. The function Π represents the application of an eighth-derivative operator to the scalar or vector in parenthesis. For some arbitrary scalar, ϕ , and vector ϕ_i , Π can be respectively expressed as

$$\Pi(\phi) = \max\left(\left|\frac{\partial^8 \phi}{\partial x^8} \Delta x^8\right|, \left|\frac{\partial^8 \phi}{\partial y^8} \Delta y^8\right|, \left|\frac{\partial^8 \phi}{\partial z^8} \Delta z^8\right|\right), \quad (12a)$$

$$\Pi(\phi_i) = \max(\Pi(\phi_x), \Pi(\phi_y), \Pi(\phi_z)). \quad (12b)$$

Finally, the artificial transport coefficients are specified in Eq. (11e). Note that in Eq. (11a) the eighth derivative operator, Π , is applied to the magnitude of the strain rate tensor, which is equivalent to the square root of the inner product of $S_{ij}S_{ji}$.

As discussed in Sec. II B 2, sink terms in both the momentum and energy equations [Eqs. (4) and (5)] were added to account for the unmeasured losses in the experimental facility. The loss force, Γ_{u_i} , and energy, Γ_E , variables were made time- and space-dependent by tying them to a simple ad hoc boundary layer evolution equation. This simple model was developed following the canonical laminar and turbulent boundary layer models [54,55]. By taking the time derivative of these equations and models and assuming $dx/dt \approx u_{\text{drg}}$, the boundary layer width, δ , can be shown to develop in time according to

$$\frac{\partial \delta}{\partial t} = \begin{cases} 5.0 |u_{\text{drg}}| \text{Re}^{-0.5}, & \text{Re} \leq \text{Re}_c, \\ 0.37 |u_{\text{drg}}| \text{Re}^{-0.2}, & \text{Re} > \text{Re}_c, \end{cases} \quad (13a)$$

where

$$\text{Re} = \frac{|u_{\text{drg}}| \delta}{\nu}, \quad u_{\text{drg}} = \hat{r}_i u_i. \quad (13b)$$

Here \hat{r} is a radial unit vector to the origin of the domain, which ensures that only the the portion of the velocity vector, u_i , acting along radial lines (i.e., u_{drg}) contributes to the loss terms. Meanwhile,

Re is the Reynolds number and ν is the kinematic viscosity. Note the Re above is not that relating to the instability development, but is solely related to the boundary layer along the chamber walls.

Then, assuming a drag coefficient (C_{drg}) should increase proportionally to the ratio of the boundary layer height (on each plate) to the chamber half-width such that $C_{\text{drg}} = 2C_o \delta/W$. We use this to approximate a drag, or loss, force through

$$F_L = 2C_o \frac{u_{\text{drg}} |u_{\text{drg}}| \rho \delta}{W^2}, \quad (14)$$

such that

$$\Gamma_{u_i} = -\hat{r}_i F_L, \quad \Gamma_E = \Gamma_{u_i} u_i. \quad (15)$$

Here, F_L is the per unit volume drag and loss force, W is the experimental chamber half width, and C_o is a drag and loss coefficient. C_o is one of two tunable parameters used to optimize the loss terms and validate the Euler model against experimental results. It is discussed further in Sec. III C.

C. 2D Euler model

Equations (3)–(15) make up the foundational equations applied to each of the three models used in this study. Stage 1 in this study’s model validation is the base-level simulation in Pyranda and involves solving of the 2D Euler equations. In the Euler model used in Stage 1 of the validation scheme, all of the foundational equations are applied in 2D using one or two different gas species. Additionally, the following source terms are set to 0: $\Gamma_{Y_{k,i}}$, Γ_{q_i} , $\Gamma_{\tau_{ij}}$. In other words, the mass flux, viscous stress, and heat flux are absent from the equations governing the 2D Euler model.

D. 2D RANS model

The RANS model used in the Stage 2a validation step was implemented through the use of LLNL’s RANSBox package of turbulence models [45]. RANSBox couples with the Pyranda source code to calculate the turbulent diffusivities and source terms in the turbulent transport equations. RANSbox adds these turbulent diffusivities, source terms, and transport equations to the foundational equations [Eqs. (3)–(15)] used in the 2D Euler model. The particular RANS model used for this study was a 2D K - L model, which adds turbulent transport equations for a second order velocity moment, K , the turbulent kinetic energy, and the turbulent length scale, L . This K - L model is derived from the RANS equations for a compressible, nonreacting, two-component fluid-mixture and was first implemented by Dimonte and Tipton [43].

While analyzing the results of this study, it should be kept in mind that RANS models assume fully developed turbulent flow through their derivation of the turbulent kinetic dissipation rate equation. As such, they are poorly suited to simulate transitioning flows such as the BDI since they assume an established inertial range and fully developed turbulent flow at all times [19,51,56]. Therefore, for transitioning flows such as this, one can only expect RANS to match experimental data at late times when the flow is more fully developed. Due to this inherent limitation, and the use of this RANS model with relatively few alterations, one does not expect much predictive capability when used for this relatively complex flow.

The equations governing the RANS model are the previous Eqs. (3)–(15) but with different values for all source, Γ , terms [Eqs. (16)–(20)]. Furthermore, as this is a *Reynolds-averaged* model, all variables represented in Eqs. (3)–(15) are replaced with their Reynolds, or Favre, averaged counterpart. The Favre and Reynolds average are defined in Eq. (24), but the replaced variables are, namely, $u_i \rightarrow \tilde{u}_i$, $\rho \rightarrow \bar{\rho}$, $p \rightarrow \bar{p}$, $Y_k \rightarrow \tilde{Y}_k$, and $E \rightarrow \tilde{E}$. Additional equations for transport and closure of the turbulent variables L and K are also added [Eqs. (21)–(23)]. The added equations and Γ terms are summarized below.

The added mass flux term is now expressed as the dissipation of mass flux driven by turbulent species diffusivity,

$$\Gamma_{Y_{k,i}} = \frac{\mu_t}{N_Y} \frac{\partial \tilde{Y}_k}{\partial x_i}, \quad (16)$$

where μ_t is the eddy viscosity and N_Y is the species mass diffusivity coefficient. Note that in this K - L model the turbulent diffusivities are constant multiples of the eddy diffusivity, e.g., μ_t/N_Y in the equation above. This will be true for all turbulent dissipation terms. The Γ term in the viscous stress tensor is now

$$\Gamma_{\tau_{ij}} = [C_{\text{dev}}(2\mu_t \bar{S}_{ij}) - C_{\text{iso}} \bar{\rho} K \delta_{ij}] M. \quad (17)$$

The term in brackets is better known as the Reynolds stress tensor, $R_{ij} = \bar{\rho} \tau_{ij}$, C_{iso} is the coefficient on the isotropic Reynolds stress, and C_{dev} is the coefficient on the deviatoric Reynolds stress.

$$M = 4 Y_k (1 - Y_k) \quad (18)$$

is a measure of fluid mixing in the system and varies from 0 to 1 in the interface region, ensuring the application of R_{ij} only in the region of the interface. The turbulent dissipation of energy is added through the Γ_{q_i} term and is defined by

$$\Gamma_{q_i} = M \frac{\mu_t}{N_e} \frac{\partial \tilde{e}}{\partial x_i}, \quad (19)$$

where N_e is the internal energy diffusivity coefficient and \tilde{e} is the Favre averaged internal energy, which is $\bar{p} \bar{\rho} / (\gamma - 1)$.

The Γ terms to model the losses in the facility [Eq. (15)] are still present in the 2D RANS model. Γ_{u_i} remains the same while the turbulent energy source term is added to Γ_E such that

$$\Gamma_E = \Gamma_{u_i} \tilde{u}_i + M \left(C_D \frac{\bar{\rho} (2K)^{3/2}}{L} - a_j \frac{\partial \bar{p}}{\partial x_j} \right). \quad (20)$$

The term in parenthesis represent the turbulent source contribution to the internal energy. Here C_D is the turbulent kinetic energy dissipation coefficient, K is the turbulence kinetic energy, L is the turbulence length scale, and a_i is the turbulent mass-flux velocity vector.

The two equations added to the Pyrandra equations of motion for this 2D RANS model are the transport equations for K and L . These are governed by

$$\frac{\partial}{\partial t} (\bar{\rho} K) = - \frac{\partial}{\partial x_i} \left(\bar{\rho} K \tilde{u}_i + M \frac{\mu_t}{N_k} \frac{\partial K}{\partial x_i} \right) + R_{ij} \frac{\partial \tilde{u}_i}{\partial x_j} + a_i \frac{\partial \bar{p}}{\partial x_i} - C_D \frac{\bar{\rho} (2K)^{3/2}}{L}, \quad (21)$$

$$\frac{\partial}{\partial t} (\bar{\rho} L) = - \frac{\partial}{\partial x_i} \left(\bar{\rho} L \tilde{u}_i + M \frac{\mu_t}{N_L} \frac{\partial L}{\partial x_i} \right) + C_{L1} \bar{\rho} \sqrt{2K} + C_{L2} \bar{\rho} L \frac{\partial \tilde{u}_i}{\partial x_i} + C_{L3} R_{ij} \frac{L}{K} \frac{\partial \tilde{u}_i}{\partial x_j}. \quad (22)$$

The terms on the second lines of Eqs. (21) and (22) make up the source terms for the governing equation of each RANS variable, while the terms on the first line containing μ_t constitute the convective and dissipation terms. Here N_k is the turbulent kinetic energy diffusivity coefficient and N_L is the turbulent length scale diffusivity coefficient. C_{L1} is the coefficient of L production, C_{L2} is the coefficient of L dilatation, and C_{L3} is the coefficient of L shear.

The remaining RANS terms needed to completely close the equations of motion are shown below:

$$a_i = -C_B \frac{L \sqrt{2K}}{\bar{\rho}} \frac{\partial \bar{p}}{\partial x_i}, \quad (23a)$$

$$\mu_t = C_\mu \bar{\rho} L \sqrt{2K}, \quad (23b)$$

$$\bar{S}_{ij} = \frac{1}{2} \left(\frac{\partial \tilde{u}_i}{\partial x_j} + \frac{\partial \tilde{u}_j}{\partial x_i} \right) - \frac{1}{3} \frac{\partial \tilde{u}_k}{\partial x_k} \delta_{ij}. \quad (23c)$$

TABLE II. List of the RANS coefficients and their values set by the model for the optimal RANS solution.

C_μ	C_{iso}	C_{dev}	C_B	C_D	C_{L1}	C_{L2}	C_{L3}	N_Y	N_e	N_k	N_L
1.00	0.67	0.16	0.11	1.24	6.11	0.33	0.00	6.37	6.37	6.37	3.18

Here C_B is the turbulent mass-flux velocity coefficient, C_μ is the eddy viscosity coefficient, and \bar{S}_{ij} is the deviatoric turbulent strain rate tensor.

All coefficients used in the RANS equations [Eqs. (16)–(23)] are listed in Table II and are automatically set by RANSBox through similarity analysis [45,56]. It should be noted that the C_{L3} term was set to zero because of the numerical sensitivity it created at early time, due to small values of K . This term, not typically included in the canonical K - L models, corresponds to the shear induced by the Kelvin-Helmholtz instability (KHI), which should have negligible effects early, but may cause discrepancies at later development times [56].

It must also be noted that in Eqs. (16)–(23), an overbar denotes a Reynolds-averaged quantity while a tilde denotes a Favre (mass-weighted) quantity. More specifically, for an arbitrary scalar b , these averages decompose as

$$b = \bar{b} + b' = \tilde{b} + b'', \quad (24a)$$

and the Reynolds averaged terms can be related to the Favre average through ρ using

$$\tilde{b} = \frac{\overline{b\rho}}{\bar{\rho}}. \quad (24b)$$

Finally, as this is an instability-driven mixing problem the late time, self-similar mixing-layer theory can be used to better inform the RANS model. Which for RMI at low Atwood such as this, much research have shown this to be [19,39,57–59]

$$h(t) \approx h_o \tau^\theta, \quad (25)$$

where h is the width of the mixed-layer, τ is a nondimensionalized time, h_o is an initial mixed width, and θ is a constant: the self-similar regime RM growth exponent.

For RTI flows at low Atwood, A (with constant driving acceleration), the self-similar mixed layer has been shown to grow according to [19,60–64]

$$h(t) = \alpha A g t^2, \quad (26)$$

where g is acceleration of the interface, t is time, and α is the approximately universal RTI growth constant. Both α and θ are tunable parameters in RANSBox. By changing values of these constants, which are more easily compared with experimental data, RANSBox changes all other RANS coefficients (shown in Table II) to best yield the desired RTI or RMI constant. Thus, they serve as a convenient subset of parameters for changing all RANS coefficients en-masse during the validation stage. In this work only θ is used as a tuning parameter in the RANS model to achieve agreement with the experimental data. Regarding α , the default RANSBox value was used such that $\alpha = 0.06$.

E. 3D LES Model

Implementing LES allows for the three-dimensional direct capture of the large and intermediate scales of motion in a transitioning flow, while modeling the smallest unresolved scales of motion. The LES model implemented here has been used successfully in many RMI and RTI problems before [26,51,61,65,66]. For computational efficiency, the 3D LES domain is restricted to only the mixing region of the divergent blast wave facility. A separate 2D domain covering the entire geometry is also implemented and the two solutions are coupled every time-step on the 3D domain

boundaries. This hybrid approach was compared to a full 3D domain approach and QOI results were effectively identical while the computational resources required were reduced by a factor of 8.

The governing equations for the 3D LES model are Eqs. (3)–(15), but expanded in all three spatial dimensions. The loss terms Γ_{u_i} and Γ_E are identical to those in the 2D Euler model and are described by Eq. (15). All other Γ terms are set to 0. For the 2D LES model applied outside of the 3D interface region, the solved equations are identical in all ways to those used in the 2D Euler model.

The numerical method used to obtain artificial fluid properties [Eqs. (11) and (12)] serves as a subgrid scale model for shear viscosity which becomes active when turbulent flow is unresolved on the mesh. Positivity in this term ensures that dissipation of turbulent energy, though unresolved, will mimic the physical mechanism of resolved flow albeit on a larger scale. The artificial shear viscosity also has the quality of being high-order, and will vanish with eighth-order convergence when the flow becomes resolved, leaving only physical viscosity as the relevant diffusivity. The artificial diffusivity constants in Eq. (11 e) remain the same.

IV. EULER VALIDATION

The process of validating the nonmixing 2D Euler was outlined in Sec. III A but will be detailed further here. As indicated in Fig. 2, the QOI used for optimization were BW pressure time histories recorded at four locations along the chamber, and the ensemble mean of interface trajectory data for the flat IC case. The model parameters used for optimization were the initial blast energy of the “energy pill,” E_o , and the drag and loss coefficient, C_o . Both these parameters are essentially controls on the uncertainties that exist in the model energetics.

As outlined in Sec. II B 2 unquantified losses occur during experimental runs. These losses were highlighted by initial attempts to tune the 2D Euler model using only E_o , which resulted in interface trajectories that exhibited too much midlate time movement. This indicated the presence of a loss term that varied in both time and space which could not be accounted for by simply lowering the amount of initial energy in the energy pill. Thus, an ad hoc drag model was introduced to create a time and space varying loss term, tuned using C_o . These losses (which may have included detonation energy lost to the facility’s plates and junctions, and energy lost to the developing boundary layer on the large plates), are primarily mix-model-independent. As such, they are determined independently in the Euler simulation through C_o and E_o .

The model QOIs used for comparison with the experimental data had to be obtained through two separate sets of simulations. This was because a large quantity of experimental pressure data existed only for single-gas experimental runs, i.e., the chamber was filled completely with air and the standard detonator was used. Meanwhile, the interface trajectory data were collected during separate runs using two gases, hence the interface. This means that for each set of C_o and E_o , a pair of simulations was completed: a single-gas and a two-gas Euler simulation.

For the single-gas simulations, agreement of the pressure profiles at each probe location was sought. The primary focus, however, was the matching of pressure profiles at the second and third probes, due to the fact that the interface location was between these probes. The pressure probe error between simulations and experiment data were assessed using the time-of-arrival at a probe location, as well as the pressure and amplitude history recorded at each probe.

The two-gas simulation results were assessed by comparing the flat interface trajectory data. As was already mentioned at the end of Sec. III A, the simulation data were sampled from an artificial window region in the domain, which matched the physical viewing-window in the experimental facility. In both cases, 2D fog concentration, or mixture-fraction, data was span-wise averaged to create 1D profiles of Y_H , the mass fraction of the heavy gas. The 50% location of these profiles was then recorded at each time to obtain the interface trajectory. The interface trajectory error between simulation and experimental data was estimated using the cumulative absolute difference between the simulation and experimental curves, and then normalizing by the area under the experimental

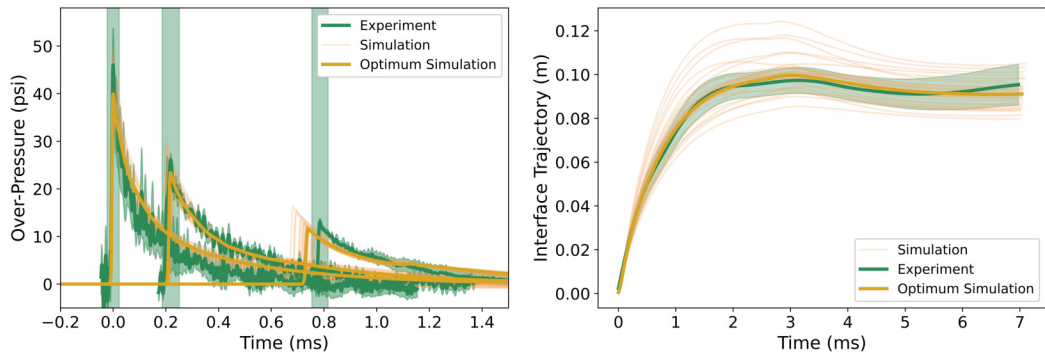


FIG. 3. 2D Euler Model: A parameter sweep in E_o and C_o is compared to experimental (left) pressure and (right) interface data. In both plots the gold solid lines indicate the ensemble mean of the experimental data, while the shaded gold region indicates the region of plus or minus one standard deviation. The black lines are results from the simulation sweep, with each line indicating a separate E_o - C_o pair. The green line indicate the simulation optimal (minimum error) solution.

curve. The results of the simulation parameter sweep as compared to the experimental data, are shown in Fig. 3.

Simulation results were compared to the experimental data and an estimate of total simulation error was made for each pair of parameters, where the error calculation for each QOI was outlined above. The total error was broken into three contributing factors. First, weighted at 25% the BW time-of-arrival error was computed using the pressure profiles. Second, and also weighted at 25% was the error resulting from the differences in peak pressure for each of the pressure probes. Last, and weighted at 50%, was the error for the interface trajectory. A parameter sweep in C_o and E_o was performed using N and M values, respectively. This resulted in $2*N*M$ calculations being computed where the relevant QOIs were generated and stored in a database. Using the total error value for each parameter pair, a Gaussian processor (GP) was used to create a high-resolution error surface for all potential parameter pairs (E_o , C_o). The GP was used to predict, and then test, the optimum pair of parameters which led to the global minimum on the error surface. The results of the GP are shown in Fig. 4.

As Fig. 4 shows, the parameter pair that was tested to have lowest error, falls nearly exactly where it was predicted to be by the GP. The gold dot in Fig. 4 corresponds to the ‘‘Optimal Solution’’ lines in Fig. 3. It should also be noted that the bold contour in Fig. 4 represents the bound on parameter pairs that would result in simulation data falling within one standard deviation of the experimental data. The fact that this encompasses a large array of parameter pairs shows that the simulation results are quite resilient to relatively ad hoc model choices. The optimal GP solution gave an E_o of 60380J and a C_o of 0.263. These values were then set as constants in the proceeding RANS and LES validation studies.

V. RANS VALIDATION

The RANS validation (Stage 2a in Fig. 2) takes the optimized parameters from the 2D Euler study, and adds a K - L RANS model to the base simulation to obtain mixing data. The specific details of the RANS model used were outlined in Sec. III D.

Ideally, a predictive RANS model would only depend on the initial and boundary conditions of the problem. The boundary conditions were set in Sec. II B 1 and here we initially introduced only two degrees of freedom by defining the initial values of L_o and K_o . These represent the modeled turbulent length scales and turbulent kinetic energy in the layer at $t = 0$, respectively. As opposed to the Euler validation, physical bounds existed for these optimizing parameters. L_o

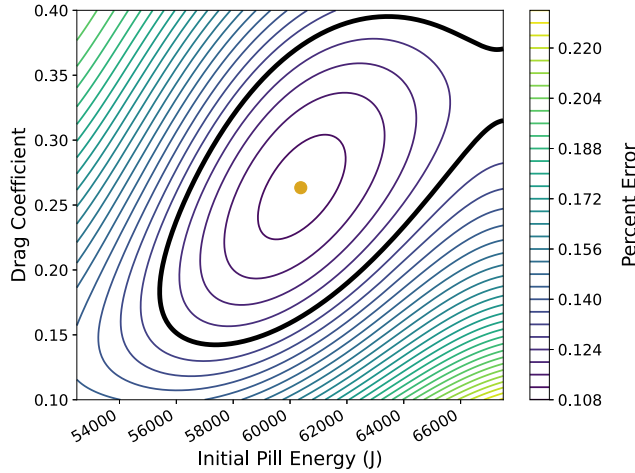


FIG. 4. 2D Euler Model: The contour of the GP error surface is shown. The orange dot indicates the realized simulation minimum, which is also the GP predicted minimum in this case. The bold contour line indicates the bounds in which a parameter pair could be selected and still produce results within the bounds of one experimental standard deviation.

must be based on a length scale that is physically relevant to the experimental problem. This meant L_o ought to only be varied from $O(1\text{ mm})$ – $O(10\text{ cm})$ as this spans the range of minimum observed initial perturbation amplitude to maximum observed wavelength. An initial RANS tuning using L_o and K_o was carried out in the same way as the Euler validation: sweeping the K_o - L_o parameter space and then feeding the results into a GP (not shown) to inform the location of more refined parameter sweeps until a combination of parameters resulted in the lowest observed error. This exercise produced good agreement with the zeroth-order experimental mixing data (W), but was unable to adequately reproduce the observed behavior in turbulent kinetic energy (see dotted black lines in Figs. 5 and 6). These results (produced with $L_o = 0.017$ and $K_o = 0.10$) are discussed more later on, but their inability to more agreeably reproduce the turbulent kinetic energy data led to a second attempt at RANS tuning by introducing a third tuning parameter.

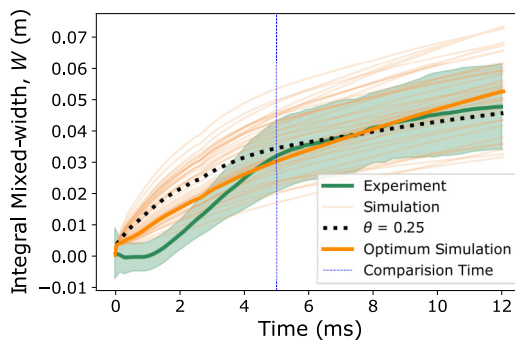


FIG. 5. 2D RANS model: Mixing data results from a parameter sweep in K_o , L_o , and θ . The optimized solution predicted by the GP is shown as the bold orange line, experimental data is shown in green and all other parameter sweep results are in light orange. The dashed vertical line indicates the time after which the simulation and experimental data were compared for RANS optimization. The dotted line indicates the optimal solution with θ fixed at the default model value (0.25).

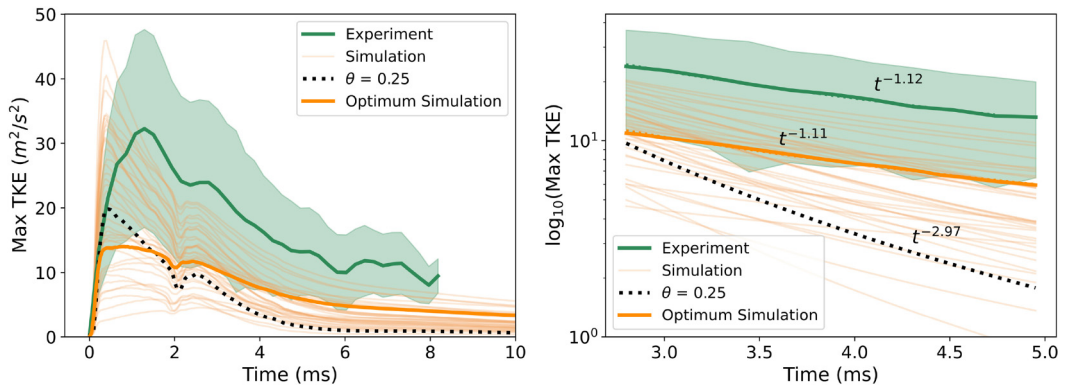


FIG. 6. 2D RANS model: TKE results from the parameter sweep in K_o , L_o , and θ . The optimized solution predicted by the GP is shown as the bold orange line, experimental data is shown in green and all other parameter sweep results are in light orange. The dotted line indicates the optimal solution with θ fixed at the default model value (0.25). (Left) The plot shows the maximum TKE of the experiment to be quite a bit larger than the simulation’s optimal solution. (Right) The plot shows the portion of maximum TKE (2.25–5 ms) used to compare the decay exponent (Φ) of maximum TKE. This is plotted in \log_{10} scale so that lines with identical decay exponents have identical slopes. The optimal solution and experimental slopes agree very well, as indicated by the Φ values shown on the plot.

As was mentioned in Sec. III D, the usage of RANS models for predicting transitional flow is ubiquitously difficult and can lead to over-fitting of experimental data, which is certainly the case here. However, RANS calculations can accelerate the design process and useful physical insight can still be gleaned in the process. To allow for the broader range of RANS solutions to be explored, we introduced an additional degree of freedom which captures variations in the RANS model itself, through the self-similar RM growth exponent θ . Variation in this parameter, will impact the coefficients in Table II according to Morgan and Wickett [67] and therefore alter the RANS model behavior.

Physical reasoning and a survey of the literature also lend credence to tuning of θ . For instance, one might not expect the same θ as was found in Morgan and Wickett [67], or other RMI focused studies. The physical problem studied in those works (solely RMI) is quite different than the flow studied in the current work, where experiments show that the BDI behaves as a combined instability not yet examined in the literature [47]. Further, based on existing RMI literature from the past two decades, a set value of θ has not been established [11,30,58,68,69]. If the value of θ has not yet been fixed after such extensive study, then it seems reasonable to allow for tuning of that parameter in this work. Thus, the tuning of θ was bounded by the range of values reported in the literature: 0.21–0.66 [11,30,58,68,69].

Optimization of the parameters L_o , K_o , and θ occurred in a similar manner as the Euler validation: for a given parameter set, error was calculated for each QOI between the simulation and mean experimental data. The parameter sweep in this case used N, M, P values for L_o , K_o , and θ , respectively, resulting in $N \times M \times P$ 2D RANS simulations being run. Again a GP was used to fit the data and produce a high resolution error surface, now in 4D. Additionally, the QOIs and their respective error measurements were also different.

The primary QOI used to assess the models ability to capturing the mixing process was the integral mixed width, W , found for experiment and simulation following

$$W = \int 4 \langle Y_H \rangle \langle Y_L \rangle dy, \quad (27)$$

where the angled brackets represent averaging in the spanwise (horizontal) direction. By conservation of mass the light gas concentration and mixture-fraction is assumed to be $Y_L = 1 - Y_H$. The 4 is to force W to one at the 50% mixture-fraction region of the mixing zone. In the experiments, the fog used in the Mie Scattering diagnostic is assumed to trace the heavy gas mixture-fraction Y_H . The intensity of pixels in each image, is then directly proportional to Y_H . While, strictly speaking, this Mie Scattering technique is qualitative, we use the scattered intensity and the integral value given by Eq. (27) as a reasonable proxy to the true mixed width. This assumption is passable in this case because the QOI evaluated is an integrated value. The mixture-fraction field is spanwise averaged at each time, and the resulting 1D profiles are integrated according to Eq. (27) to obtain a single value for W at each time step. The time-dependent $W(t)$ of each experimental run is then averaged together to obtain the data ensemble used for simulation comparison. An identical process is used to acquire W data in the RANS simulation. The Y_H fields are averaged and integrated at each time to get the $W(t)$ resulting from a combination of simulation parameters, which can then be directly compared to its experimental counterpart. This RANS-experiment comparison is shown in Fig. 5. One should note the good agreement found between the experiment and the initial RANS model tuning (black-dotted line), where θ was held fixed at 0.25.

The integral mixed-width error was calculated using the integrated absolute difference between simulation and experiment (just as in the Euler interface trajectory error), but only for a selected time range of the simulation. The first 5 ms after the blast are neglected in the error calculation since the RANS model always assumes a fully turbulent flow where in actuality, the flow is transitional in this region. This explains the early time discrepancies between simulation and experiment in Fig. 5.

The second QOI used in the RANS validation was the turbulent kinetic energy. It should be noted that we will generally refer to turbulent kinetic energy as “TKE.” However, the TKE values produced by the RANS model will be referred to as K , while the experimental TKE values will be k . This distinction is made because these values are closely related but not necessarily precise analogues, as will be discussed here.

The high-speed experimental PIV data, which produces the k data, was acquired from experimental campaigns separate from the Mie Scattering campaigns used for all other experimental QOI in this chapter. As a result, the camera field-of-view was different for the two of these campaigns, and was notably smaller for the PIV/ k data. So, a second artificial window was used in the simulation to extract all data that was compared with experimental PIV data. The RANS model’s turbulent energy transport variable, K , was spanwise averaged in this smaller PIV window, and then the maximum value of each spanwise average was recorded to obtain the temporal development of maximum K .

This was compared to the experimental TKE values (k), which were computed as follows: 2D fields of velocity vectors were produced using the Davis software from LaVision. The spanwise average components of velocity were then subtracted off the velocity field at each time-step to obtain a field of velocity fluctuations (v' , u'). These fluctuating quantities were then used to compute a 2D field of k values. Note that due to the assumptions inherent in the RANS model, the K variable it produces must be interpreted as the 3D turbulent kinetic energy, despite the 2D nature of the simulation. Thus, to make a comparison to this metric, the 2D experimental data must be modified to create a proxy for the 3D TKE (K). This is done by assuming $w' \approx u'$, such that

$$k = 0.5\sqrt{2u'^2 + v'^2}. \quad (28)$$

The experimental k field was then spanwise averaged and recorded in the same process as that of the simulation outlined above. However, an additional difference is that the K variable produced by the RANS model assumes a Favre-averaged definition of TKE. In other words, the RANS model outputs a density weighted K , which influences the magnitude of the value. In this work, the influence of Favre-averaging on the magnitude of K is assumed to be small. For all of the reasons just outlined, it can only be reasonably expected that, at best, $k \approx K$. These facts are likely a large reason as to why no simulation solutions match the experimental maximum TKE well in Fig. 6(a).

Due to the large discrepancy in TKE magnitudes caused by the differences in k and K , the TKE magnitude is not used for the error comparison. Instead, because the energy dissipation rate (ϵ) is determined by the power-law exponent (Φ) of the TKE decay, this exponent is used to compare experiments and simulation. In other words, because $\epsilon \propto t^\Phi$, a match between $\Phi_{\text{Experiment}}$ and Φ_{LES} was sought. The decay exponent was only computed during the time range of relatively smooth maximum k decay in the experimental data (from about 2–6 ms). This was selected because it occurs after the small dip in TKE observed in both experiments and simulations. This dip is due to reflected waves, caused by the incident blast-wave passing through the interface, interacting with reflected waves coming from the bottom floor of the facility. The two reflections are initially propagating in opposite directions, but upon collision the resulting acoustic and pressure wave propagates in the direction of the interface. The interaction of this wave with the interface causes the dip in maximum TKE seen in Fig. 6(a) at ≈ 2 ms. A power law was fit to the data after this interaction, and the resulting exponent of the experiment was used as the target value for RANS optimization and error evaluation. As can be seen in Fig. 6(b) the optimal solution and experimental slopes agree very well, despite the large difference in magnitude. This indicates that the TKE decay exponent in the optimal simulation and the experiment match well, meaning the rate at which they dissipate turbulent energy is nearly the same.

The error from the mixed-width and TKE data were each weighted at 50% to create the total error that was then more finely sampled using a GP. As mentioned previously, because three optimizing parameters were used (K_o , L_o , θ) the resulting GP error surface is 4D. The minimum error location on the 4D surface was recorded as the optimum solution. The three planes intersecting the error surface at that point are shown in Fig. 7. Note the values for K_o are given as $\ln(K_o)$ due to the large range in values (10^{-5} – 10^{-1}) used in the parameter sweep. The lack of variation in K_o , however, indicates that the model is relatively insensitive to large changes in the initial turbulent kinetic energy. Additionally, the relatively large array of parameter pairs located within the bold contour in Fig. 7 indicates the RANS model is also quite resilient to model choices.

A note should be made concerning the optimal RANS solution. The optimized value of $\theta = 0.525$, is relatively high in comparison to the values reported in RMI literature, but higher values have been previously reported for transitioning flows (e.g., Groom and Thornber [70] and Sewell *et al.* [69]). However, setting this value in the RANS model does not enforce the RMI power law behavior from which θ gets its name. Indeed, the RANS model detects and responds to finite baroclinic torque, so the RT unstable portion of the BDI will induce appropriate changes (increases) to θ and mixing rate.

Physically, an increased θ also corresponds to a slower rate of TKE decay as compared to a traditional RMI flow. This is certainly the case in the BDI as the effects of the combined RTI cause further vorticity deposition, and thus more TKE, which can then be sustained longer (i.e., decay slower) due to this second instability. In fact this was observed in the first RANS tuning with $\theta = 0.25$. Figure 6 shows that the initial optimal solution produces a much faster rate of TKE decay than that of the experiment. This is likely due to the relatively low default value of θ (0.25) in the RANS model.

The RANS model was expected to have limited predictive capabilities when applied to this problem set up. However, despite these inherent limitations and the minimal model alterations, the RANS model was able to reproduce certain characteristics of the experimental data with some success. Albeit, we interpret the need to tune θ as an indication of the limitations of the RANS model and thus do not suggest the general applicability of such a tuning.

Finally, when regarding the multistaged validation approach of this work, it is fair to wonder whether parameters can be independently tuned in each stage. For instance, in a worst case scenario the C_o parameter tuned in the Euler validation could feasibly couple nonlinearly with the tuning parameters used in the RANS validation portion. Interactions like this would mean that all parameters ought to be tuned simultaneously in a high-dimensional space.

To acquire direct evidence whether parameters could be tuned at different stages in the way proposed, another exercise in RANS optimization was completed, this time allowing for variation

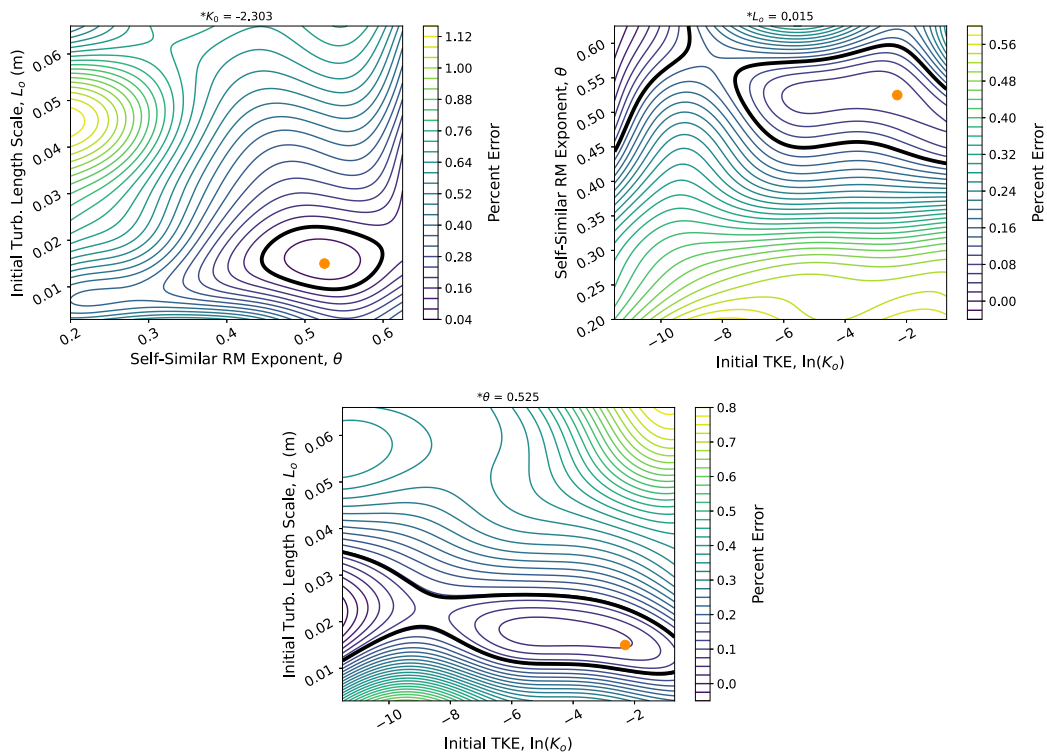


FIG. 7. 2D RANS Model: The three intersecting planes of the 4D error surface resulting from the RANS GP routine. Note that in each contour plot, two of the optimized parameters are varied, while the fixed and optimal value of the third is indicated at the top of the plot with an asterisk. It should also be noted that the values for K_o are given as $\ln(K_o)$ due to the large range in values (10^{-5} – 10^{-1}) used in the parameter sweeps. The bold contour line in each plot is once again used to indicate the parameter space which results in simulations within 1 standard deviation of the experimental mean. Clockwise from top left: θ vs L_o , K_o vs θ , and K_o vs L_o .

in the E_o and C_o parameters used in the Euler model. The starting point of this optimization was the optimal RANS parameter values found above, and a space $\pm 25\%$ of the optimal Euler parameters. This suite of runs was then analyzed against the experimental results in the same way outlined above. The results showed that the combination of parameters yielding the minimum error, was the same as those reported above. That is, the optimal solution was the same as that shown by the bold lines in Figs. 5 and 6. In other words, the parameters found in the multistage process are at least in a local minimum of the larger multidimensional parameter space where nonlinear interactions between different model parameters likely do not exist.

VI. LES VALIDATION

The LES validation (stage 2b in Fig. 2) takes the optimized 2D Euler parameters as inputs and solves Eqs. (3)–(15) but expanded in all three spatial dimensions. The numerical method for artificial fluid properties [Eqs. (11) and (12)] serves as an implicit subgrid scale model for scales smaller than the mesh.

As opposed to the previous validation stages the LES validation requires statistically representative IC information as a model input. This was done using two different approaches. The first method obtains an accurate experimental representation by collecting Mie Scattering snapshots of ≈ 300 “typical” ICs. Parts of the first IC characterization process are shown in Fig. 8, where the

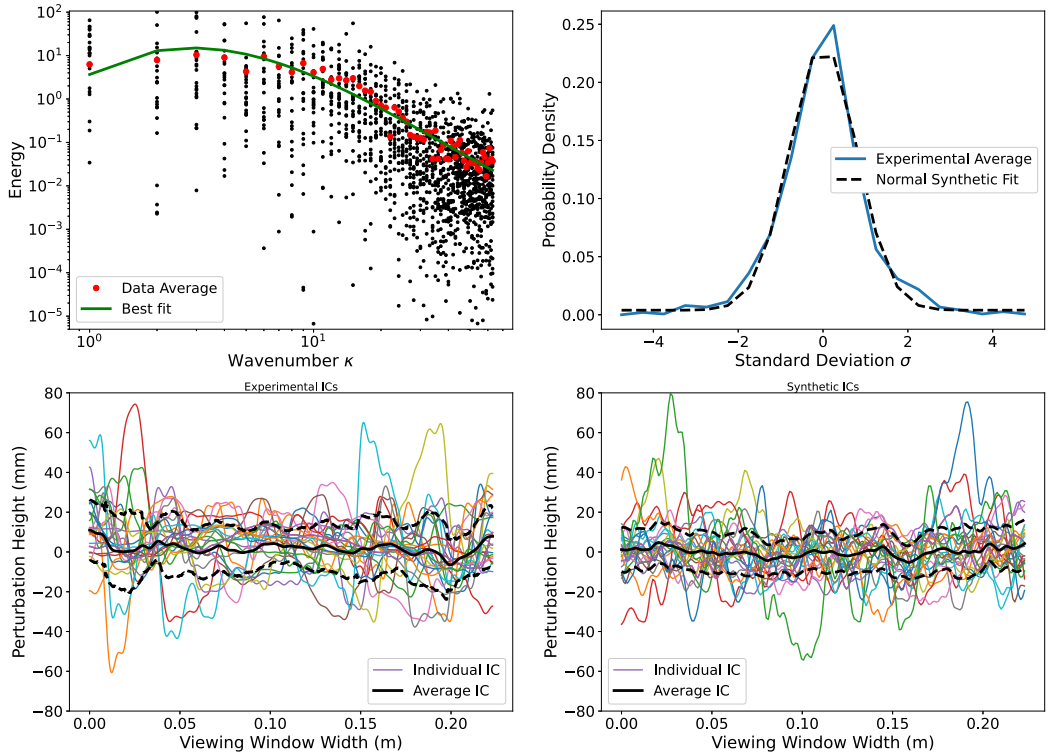


FIG. 8. 3D LES model: Data used in the first IC characterization process. Bottom left—IC shapes from 30 of the 300 images. The mean of the ensemble is shown as the black line, along with one standard deviation. Top left—The result of the DCT for each of the 30 ICs. The red dots show the average energy in each mode, and the line of best fit is shown in green. Top right—The average distribution of energy found at each wave number (blue line). The dotted black line shows the distribution fit to the data. The fit distribution is a combined normal and uniform PDF. Bottom right—30 synthetic ICs resulting from the random sampling of the distribution at each wave number.

plots are shown with data from only 30 of the 300 IC images for better clarity. The first step in the characterization was to obtain an interface shape from each of the IC snapshots by identifying the pixel location corresponding to the maximum gradient of pixel intensity along each column of the image. The resulting 1D array of the interface “shape,” when overlaid on the 2D IC image, traces the interface between the two gases well. Interface shapes from the experimental images are shown in the bottom left of Fig. 8. Next, a discrete cosine transform (DCT) is performed on each of the 300 IC shapes to acquire the energy spectra as a function of wave number, κ , for each experimental IC. The DCT provides information about which “modes,” or κ , contain the most energy for each IC. The first two modes were removed from each spectra as they corresponded to the mean interface shape (flat), and a “smile shape” caused by the camera lens’ barrel distortion effect at the bottom of each image. A line of best fit is then acquired from this data, as shown in the top left of Fig. 8. The average and standard deviation of the DCT coefficients are then computed for each mode, and are then used to compute a probability density function at each mode/ κ . The distribution created by the IC data was then fit to a combination of a normal and a uniform distribution, an example of which is shown in the top right of Fig. 8. Thus, the line of best fit found for the DCT coefficients essentially sets the mean of each distribution for every resolved wave number. In other words, a PDF exists along the Best-fit line in the top left of Fig. 8 for each wave number.

With a distribution of DCT weights and coefficients at each wave number, synthetic ICs can then be generated by cycling through each mode and selecting randomly from the distribution at that wave number. With a randomly selected DCT coefficient for each κ , the inverse DCT can be performed to generate a synthetic IC shape which would be statistically equivalent to a typical experimental IC shape. Resulting synthetic ICs are shown in the bottom right of Fig. 8. However, because 3D ICs are needed for the LES validation, the κ -dependent randomly selected DCT coefficients are projected to 2D cosine space, and then inverse transformed. The lowest κ available in the third-dimension is limited by the physical dimension of the chamber, but the energy in all higher κ was determined by selecting from the distribution of DCT coefficients used previously. This creates a 3D surface of synthetic perturbations that can be overlain on the interface location in the 3D domain. In other words, the out-of-plane perturbations are based on statistics of those in plane (2D images), with the added constraint that any given perturbation cannot be larger than the chamber depth. This was done 27 times to generate 27 synthetic ICs to match the number of experimental realizations used in the study.

During each of the 27 LES runs, the 3D interface evolves differently due to the random, yet statistically representative, IC generated for each. A 3D evolution for one of the 27 LES runs is shown in Fig. 9. The isocontours shown in the figure represent the volume fraction of the more dense fluid, Y_H . The 3D IC is shown at the top of the figure immediately before BW interaction, which travels upward in the figure's frame of reference. In the moments after blast interaction, one can note the apparent compression of the IC initial amplitude. This is caused by the phase inversion, in which initial peaks become valleys (and vice versa), caused by the BW propagating from a more to a less dense gas. Another marked feature is the initial stretching of the overall interface length. The BW forces the interface upwards, and due to the diverging geometry the interface stretches to conserve mass. In addition to the stretching due to geometric effects, the deposition of vorticity due to the subsequent RM and RT instabilities causes local stretching at perturbation sites. By ≈ 2 ms the interface amplitude has inverted back to its initial amplitude, and more than doubles in size in the next 2 ms. This roughly marks the transitions from the exponential growth of the linear phase, to the linear-in-time amplitude growth of the nonlinear phase. The beginnings of vortex roll-ups caused by KHI can also be seen at several spike and bubble tips at 3.5 ms. By 7 ms the volume fraction isocontours begin to collide and merge until a turbulent mixed layer appears to be reached at 11 ms.

To make apples-to-apples comparisons between the 3D LES simulations and the experiment, the central plane of the 3D LES domain was used to collect all data for comparison with experiment. For example, the 2D slices of heavy gas volume fraction, Y_H , taken from a 3D data set exemplified by Fig. 9, were used to compute the integral mixed width (W) for experimental comparison.

An example of the temporal evolution of 2D slices are shown in comparison to experimental Mie scattering images at identical development times in Fig. 10. The IC immediately before blast impact is shown as the far left image for the LES and experiment. One immediately notices the more diffuse nature of the simulation compared to the experiment. This may be primarily due to the numerical diffusion acting at scales below the grid resolution. In the 3D domain the limiting resolution is in the horizontal and depth directions. Because the data was taken on 2D slices of the 3D domain, the depth resolution is essentially irrelevant. In the horizontal direction the 27 LES runs were performed with 512 grid points across, giving a grid spacing of about 1 mm. In contrast to the experimental resolution (≈ 0.1 mm between image pixels) this is quite coarse, so it should be kept in mind when making comparisons.

During the first several ms of the developments shown in Fig. 10 the perturbations grow similarly. A range of perturbation sizes can be seen in both LES and experiment, although more small perturbation features can be seen in the LES. The beginnings of spike tip roll-up, or KHI development, can be seen in each row as early as 2 ms. Another feature of note is a vortex pinch-off event observed in both. In the LES: the top of the large spike seen at the bottom of the LES image is starting to separate from the main spike body at 4 ms and becomes detached at 6 ms. A similar event is observed in the experiments if one tracks the second large spike down from the top of

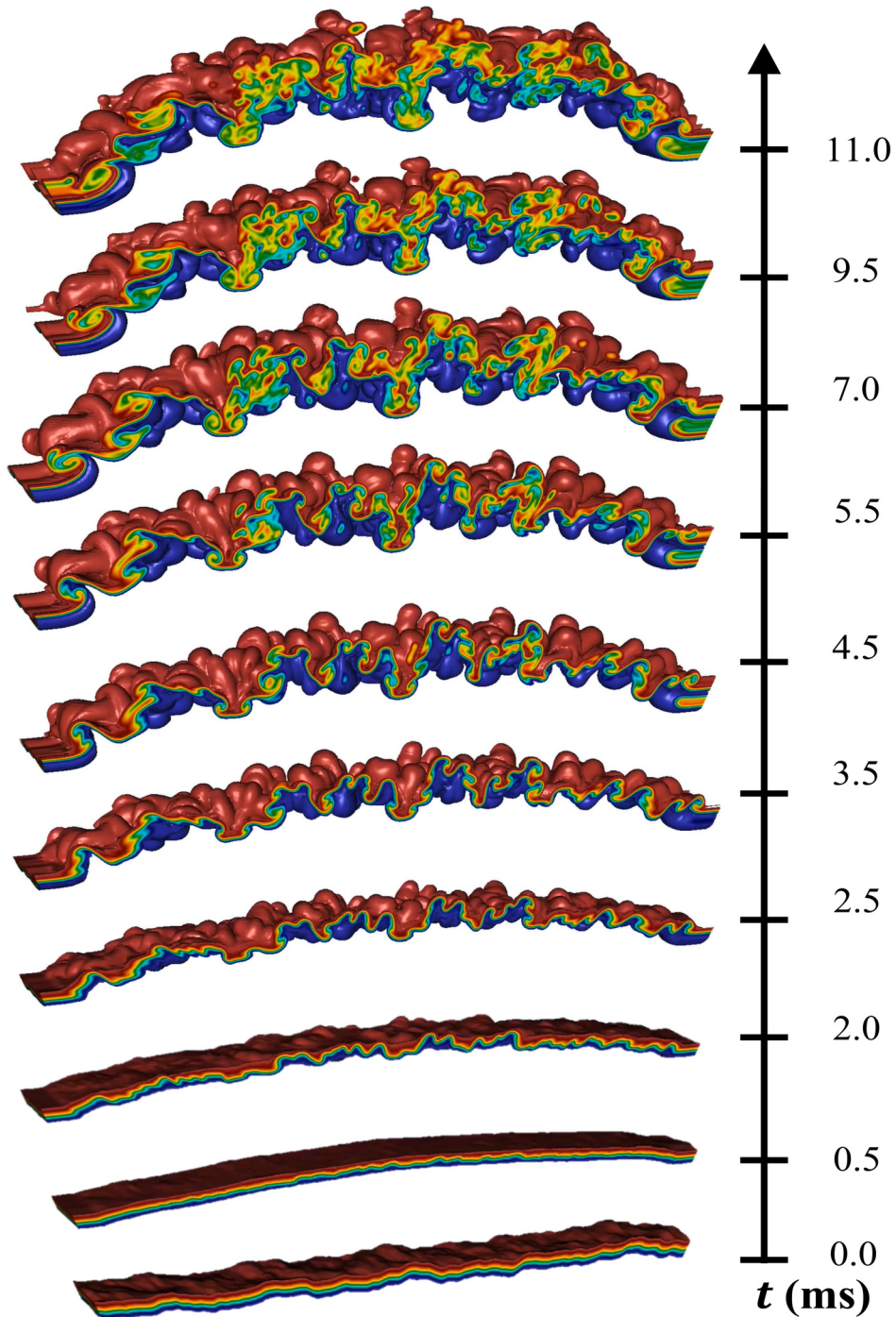


FIG. 9. 3D LES model: A temporal 3D evolution of the Y_h volume fraction field starting from a statistically representative and randomly generated IC. The time axis is shown on the right-hand side, with the IC located at the bottom ($t = 0$). The blast wave propagates up from below the IC and deposits vorticity to cause the development seen for $t > 0$. Note the stretching of the interface length as it moves up the diverging chamber. See Supplemental Material [71] for a video of this 3D LES development.

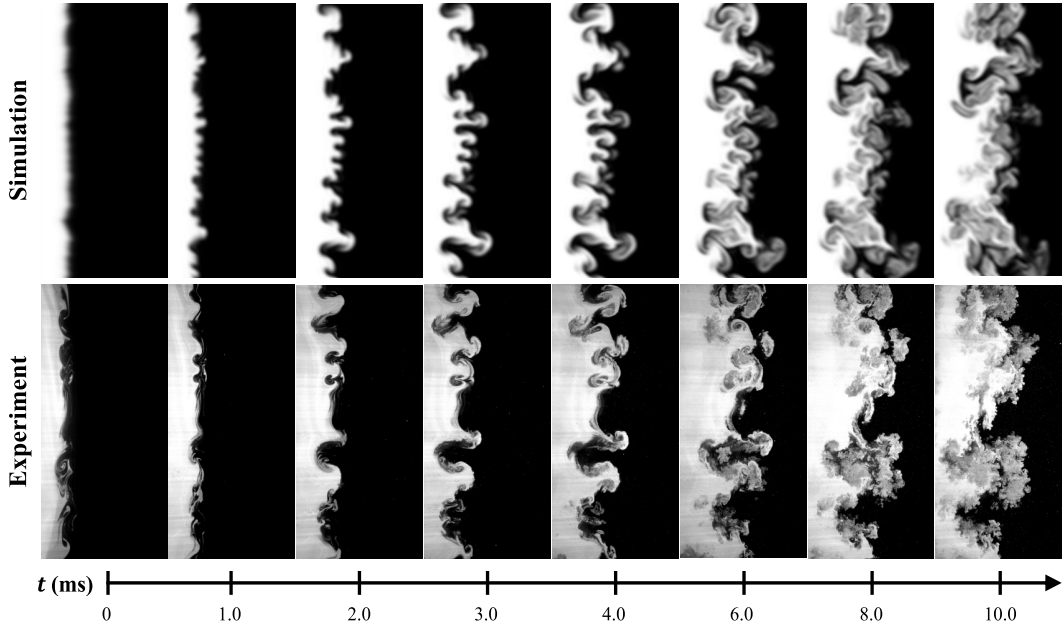


FIG. 10. 3D LES model: A comparison of the temporal evolution of the 2D Y_h fields for a slice of the 3D LES and versus the experimental Mie Scattering. Each field is taken from an individual LES or experimental run. The far left figure is the IC immediately prior to BW interaction. The indicated times (in ms) after blast interaction are identical for LES and experiment. The images have all been rotated 90° and cropped to include only the mixing layer at each time step to allow for a better comparison of the instability development. The BW propagates from left to right in the shown orientation and the bulk interface motion, which has been cropped out, is in the same direction. See Supplemental Material [71] for videos of the 2D LES and experimental Mie Scattering development. Note the two videos are not to scale in size or playback time, and are from different runs than those shown in the images above.

the experimental images. The tip of the vortex begins to separate at 3 ms and is seen to be clearly separated by 6 ms. The fate of this feature in the experiment is different from that of the LES in that it breaks up into much finer scales than can be seen in the LES. This is generally true for all features in the LES versus experiment, as the finer structure in experiment indicate the higher Reynolds number of the flow and the limited resolution of the LES on those scales.

One can also note the more frequent occurrence of secondary instability in the experiment as compared to the LES images. This could be due to the fact that the LES is not resolving small scale perturbations that may be seeding these secondary instabilities. A very similar phenomenon was observed in Morgan *et al.* [51] when comparing Mie Scattering experiments with Miranda LES results. The minimum interface thickness (essentially the grid spacing) necessitated by the simulations may also inhibit the secondary instabilities by effectively smearing out the gradients needed for them to develop. The disparity between the experimental scales of motion and those of the simulation is simple (at least notionally) to reduce and one need only to increase the spatial resolution of the computational mesh. This can become cost prohibitive rather quickly and as we will show later, was not needed to capture the desired QOIs.

The ensemble data comparison between the LES (using the first IC characterization method) and experiment for W is shown in Fig. 11(a). W is found using Eq. (27) in an identical manner as the experiment. To make a direct comparison between the experimental 2D $W(t)$ and 3D LES results, the central plane of the 3D domain was sampled (as if it were the laser sheet in the experimental set-up), and the procedure matching that of the experiment was followed, which was outlined in

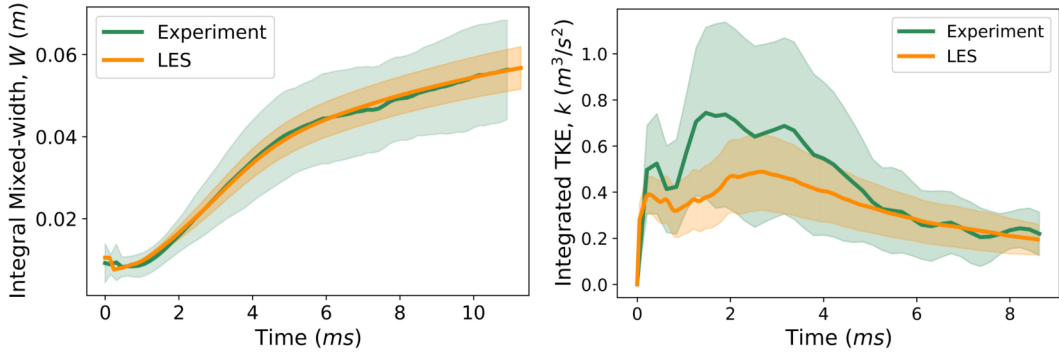


FIG. 11. 3D LES Model: The ensemble comparison of (left) integral mixed width (W) and (right) integrated TKE (k). The LES ensemble data was found using the first IC characterization method. The mean of each ensemble is shown as the bold line, while the spread of results in each ensemble is represented by the shaded region which indicates \pm one standard deviation from the mean.

Sec. V. In this way the LES results can be thought of as 2D slices of a 3D data set, in the same way that the experimental data is taken from a 2D laser sheet that is sampling what is at best a quasi-2D flow field. Figure 11(a) shows that the $W(t)$ ensemble means of LES and the experiment show excellent agreement, with only a slight deviation at late times. There is also evidence of small disagreement immediately after passage of the BW, as the experiment shows a slightly more prolonged exponential (linear) growth phase than that of the LES.

However, the LES does quite poorly in capturing the spread of the experimental $W(t)$ ensemble, as is shown by the shaded regions which show \pm one ensemble standard deviation from the mean. There could be multiple reasons for this behavior, one being that this first IC characterization method does not properly capture the amount of variance present in the experimental ICs. This would lead to LES solutions more tightly packed about the mean. Another reason could be due to the inherent nonlinearity in the system, which causes heightened sensitivity to initial conditions. Small differences in the synthetic versus experimental ICs could lead to large changes in the ensemble spread. Or, if the ICs are indeed adequately characterized by the synthetic ICs, then the LES may not be replicating the high degree of nonlinearity in the experimental system. This can be observed to some degree in the IC images of Fig. 10, where the experimental image shows a much higher-degree of nonlinearity in the wisps, sheets, and small vortices that are not adequately captured by the LES image.

The LES results using the first IC characterization method are also compared to the experimental velocity (PIV) data. To make the most direct comparison to experiment, the central slice of the the 3D LES data was again taken to acquire a 2D LES velocity field in the middle of the domain. The LES velocity field was then mapped to a grid with a vector resolution matching that of the experiment (0.375 mm/vector). The “window” on this interpolated grid was also matched such that the LES and experiment would have the same field of view. The resulting velocity fields can then be directly compared and processed. Thus, as opposed to the RANS validation, the LES validation can directly compare the k produced by experiments to that of LES.

LES velocity fluctuations were mapped to the matching experimental grid and then used to obtain a 2D field of k , which was then spanwise averaged to obtain a 1D k profile for each time step in the evolution. The spanwise k was then integrated in the stream-wise (vertical) direction to obtain integrated TKE (units m^3/s^2) for each time. This was repeated for each of the runs in the ensemble to get the mean integrated k development in time. The comparison of this quantity for LES and experiment is shown in Fig. 11(b). Note that in this approach the w' component of velocity for the LES was approximated to be u' , just as is done for the experiment, despite the fact that the 3D LES data produces actual values of w' . Thus, the k variable produced by experiment is reproduced

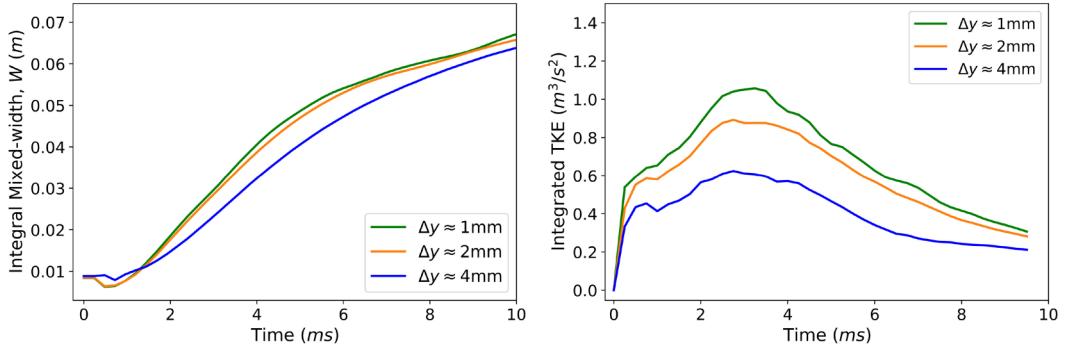


FIG. 12. 3D LES model: The comparison of (left) W and (right) integrated TKE for LES runs with the exact same IC, but different grid resolution. Because the variables are spanwise averaged, the resolution in the vertical direction is shown. The resolution of the LES ensembles is equivalent to the $\Delta y \approx 2$ mm case shown here. The plot of W indicates near grid convergence, while the integrated TKE plot shows a lack of convergence even for a doubling of resolution.

exactly the same in the LES data, allowing for more direct comparison between data sets. Note that this k variable is not technically considered turbulent kinetic energy, but is just an approximation of that variable.

The comparison of k in Fig. 11(b) shows that the LES ensemble mean does not capture that of the experiment as well as it did for W . This is likely partially due to grid-dependent effects. Because TKE is a second-order statistic, it is more sensitive to grid resolution than the zeroth-order W . Thus, it requires higher resolution to show grid convergence, whereas the LES results for W may have already converged. One would expect that running the LES ensemble at a higher resolution would bump the integrated TKE values up noticeably. Unfortunately, limited computational resources prevented the authors from performing another 27 case ensemble of 3D LES simulations at double the resolution, which equates to $16\times$ the computational expense.

Nevertheless, one can explore the effect of grid resolution on a specific LES run. This is shown in Fig. 12 where the affect of increasing grid resolution can be seen for W and k . As can be seen in Fig. 12, increasing the resolution has a much smaller effect on W [a (left panel)] than it does for k [b (right panel)]. For W , the results show that the resolution used for the LES ensembles ($\Delta y = 2\text{mm}$) produces results essentially the same as those which are twice as resolved. This indicates that for W , the ensemble results are nearly grid-independent and should not change for a finer resolution.

However for k , a doubling of resolution from that of the ensemble results in a notable increase in integrated TKE, as seen in Fig. 12(b). This means that the TKE data produced in the LES ensemble has not yet converged. Therefore, increases in resolution should indeed push up the magnitude of k seen in Figs. 11(b) and 14(b), indicating that at least part of the discrepancy between the LES and experiments is due to inadequate resolution in the simulations. In fact, even a doubling of the LES resolution would still not achieve the vector resolution of the PIV experiments ($\Delta y = 0.375$ mm), or grid independence, as can be seen in Fig. 12(b). Clearly the fine scales of the flow are under-resolved, and capturing the additional energy contained in them would likely require significantly more resolution.

The effect of increased resolution can also be qualitatively examined by investigating the changes to the Y_H field in the central plane of the 3D LES domain. This is shown in Fig. 13. As can be seen, there is a small but distinguishable difference between the three cases at all times. While the difference is more muted at the IC and immediately after BW interaction (1.5 ms), one can see that the interface increasingly appears more “crisp” with higher resolution. This is because the effective density gradient across the interface is becoming steeper with increase in resolution. In turn, the finer density gradients result in more vorticity deposition. This vorticity is deposited at the scale at

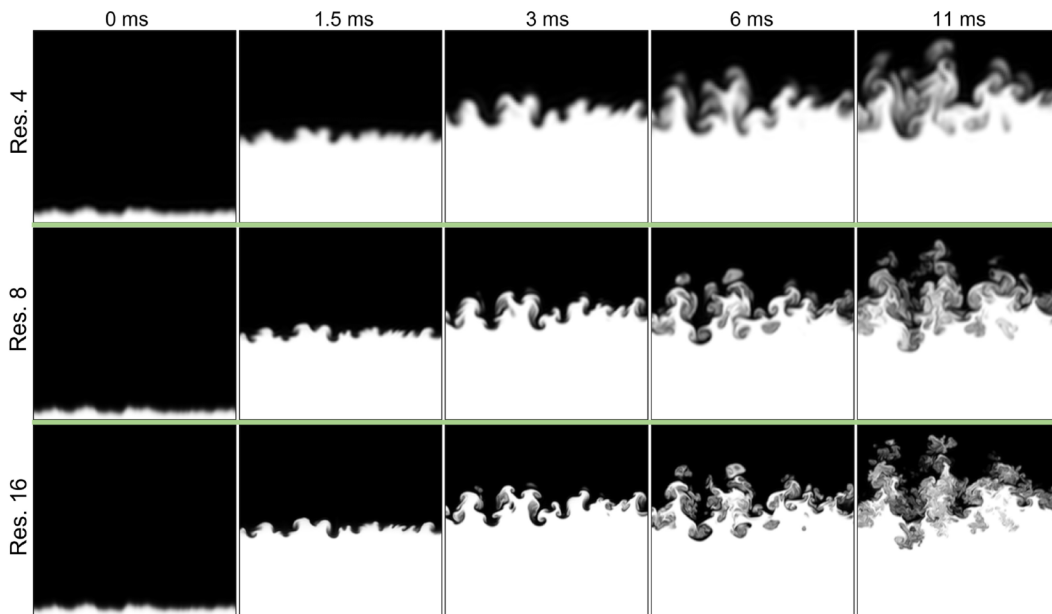


FIG. 13. 3D LES model: A comparison of the Y_H fields for the exact same IC, but at different resolutions. The Res8 case corresponds to the resolution at which the LES ensembles were produced. Res4, Res8, and Res16 correspond to vertical resolutions (Δy) of 4 mm, 2 mm, and 1 mm, respectively. Time proceeds from left to right.

which the pressure and density gradients exist. As a result, the finer density scales present at higher resolution create finer scales of baroclinic torque, but not large scales of motion that would alter the mean flow. This is why, on the largest scales, the runs look so qualitatively similar despite the increase in resolution. However, this increase of resolution-dependent vorticity deposition at the small scales is likely a primary contributor to why the relatively under-resolved LES ensembles result in lower TKE magnitudes when compared to experiments [Figs. 11(b) and 14(b)].

During later times, the difference in resolution manifests itself as the appearance and generation of these smaller scales. For instance, at 11 ms the Res16 case shows a range of scales that look much

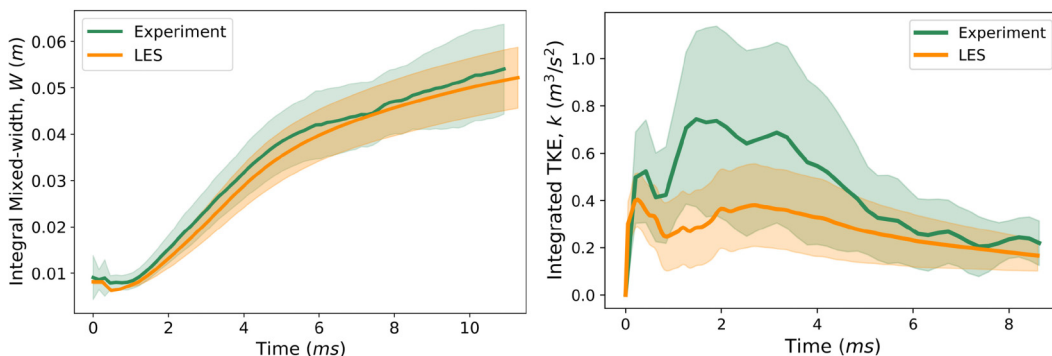


FIG. 14. 3D LES Model: The ensemble comparison of (left) integral mixed width (W) and (right) integrated TKE (k). The LES ensemble data was found using the second IC characterization method. The mean of each ensemble is shown as the bold line, while the spread of results in each ensemble is represented by the shaded region which indicates \pm one standard deviation from the mean.

more characteristic of a turbulent state than the other two resolutions. These fine scale structures also serve to slightly change the shape of larger structures between the three cases. In general, an increase in resolution seems to allow for more “jagged” coherent structures, while the lower resolution effectively smooths out features into rounder shapes.

Finally, to test the sensitivity of the LES results to the characterization of ICs, a second IC approach was used. This was done to determine whether the first IC characterization method was leading to the smaller LES ensemble variance observed in Fig. 11(a). In the second IC characterization method, the IC images from the 27 experimental runs were used instead of the 300 image ensemble of “typical ICs.” The IC shape for each of the 27 runs was then essentially fed into the simulation so that each LES run had a counterpart experimental run with the same IC shape. For instance, the experimental IC shape (examples of which are in the bottom left of Fig. 8) for each of the runs was directly input into the LES simulation. The distributions obtained in the first IC characterization scheme were used to extrapolate the IC shape to the grid boundaries in the horizontal (outside the viewing window), and into the plane. This created a 3D perturbation for which the central slice exactly matched an experimental perturbation.

The integral mixed-width results of the LES simulations using this second IC scheme are shown in Fig. 14(a). As can be seen, feeding the IC from an experimental run directly into the LES largely increases the spread of possible results. While the mean of the $W(t)$ ensemble does not match as well as the previous approach, it is still in very good agreement. More impressively, the variance of the ensemble matches much closer than the previous results. Concerning the comparison of ensemble k data shown in Fig. 14(b), the second IC characterization does little to improve the disagreement between experiments and simulation. This may indicate that even for the second IC characterization, there is still information missing which may influence TKE development in the experiment. Further, the new ICs did little to increase the spread of simulation TKE results to a level comparable with the experiment. More work is needed to fully understand the large spread of results in the experimental TKE, but there are likely several factors at play. First is the possibility of nonlinear effects in the system not captured in the simulation, which could cause large degrees of variability in second order statistics like TKE. Second is the lower number of PIV experiments conducted (10) as compared to the Mie Scattering ensemble (27). Finally, the difficulty of performing PIV in this facility due to the high speed nature of the flow, creation of debris and soot particles from the detonation, and the limited resolution necessitated by choosing a useful field-of-view increases the experimental error in this diagnostic, which manifests itself partially in the spread of results.

These results reinforce previous findings that show how crucial IC characterization is for LES. Despite having described the experimental ICs in a way that fully described them statistically, and where the ensemble mean was in excellent agreement, the ensemble variance was largely under predicted. In the second IC characterization method, using the exact ICs from each of the 27 experimental realizations almost doubled the amount of variance present in the LES solutions, while keeping the ensemble mean nearly the same. This is despite the fact that these same 27 ICs can be described statistically by the first IC method. Indeed, due to the nonlinearity of the BDI, experiments and simulations of it are highly sensitive to ICs. Therefore for best results the LES ICs should be matched *exactly* as possible to replicate experimental behavior.

VII. DISCUSSION

This work has shown that, generally, the LES and RANS models used in this study can reproduce experimental BDI data. Notably, the validation hierarchy is novel in that it directly connects three experimental data sets with simulation in a staged approach. A fully coupled validation where all uncertainties are considered simultaneously may be more complete in accounting for complex correlations, but becomes intractable when considering the cost of full 3D LES. In addition, though we found the expected mean of certain model parameters via GP regression, the distribution of these uncertain parameters was not explored but could be in future work via Markov chain Monte Carlo

using the GP as a surrogate. This would allow model and experimental uncertainties to be fully fed forward into the QOI for turbulent mixing.

While different QOIs have displayed varying levels of success for each model, both RANS and LES seem to have captured at least zeroth-order BDI behavior. However, as expected, RANS cannot capture the turbulent transition process and therefore flows that are strongly dependent on transition will remain difficult to capture. Indeed, RANS solutions can be calibrated to match data at certain points in time or certain regions of the flow where the approximation of fully developed flow is appropriate. In the present study of BDI, a notable increase outside the normal range of the model coefficient (θ) was required to approach good experimental agreement. The reported θ value is in the upper range of reported values in the RMI literature. However, as the experiments provided significance departures in geometry and instability dynamics as compared to typical RMI flows, this is unsurprising. Indeed, departure from canonical flows and geometries will likely require further investigation of RANS model coefficients to achieve favorable results.

Comparably, while the 3D LES model was able to capture the zeroth-order mixing behavior of the BDI quite well, it was too under-resolved to replicate high-order velocity statistics. Further, even on the zeroth order, it was shown to be sensitive to the method by which experimental ICs were reproduced. This observation underscores both the high nonlinearity of instabilities such as BDI, but also the importance of IC characterization in LES studies.

The run-to-run variation of the BDI experimental mixing data was large and therefore necessitated a large ensemble to reasonably bound the mean behavior. This variability is expected given the strong dependence and persistence of the ICs on the flow which is in large part due to the dominant two-dimensional flow of the facility. That is, only the finer scales become turbulent at this Atwood number. Likewise, it is reasonable to expect that simulations capturing the same narrow 3D extent would exhibit the same strong variability to ICs. This was directly observed in the present study and shows a strong need (if not requirement) for instability-driven mixing which depends largely on their initial conditions to be conducted as ensemble studies. Otherwise, the utility of individual results will be limited to the narrow scope of those particular ICs [58]. To the authors knowledge, the level of comparative rigor exercised in this study for shock-driven mixing (where ICs were point-wise matched, post-processing was identical, ensembles were used, etc.) is unprecedented.

The LES and experimental data can be used further to investigate the unique mixing evolution of the BDI. Three distinct mixing regimes can be identified by looking at the integral mixed-width growth rate, \bar{W} , for both LES and experiment seen in Fig. 15(a). The growth rate matches in both magnitude and general shape, where large changes in growth rate (regimes) are seen to occur at the same time in LES and experiment. For instance, the initial negative growth rate at the earliest of times displays the ability of the LES to capture the phase inversion which the BDI undergoes (due to the BW passing from higher to lower density fluid) [47]. This inversion is challenging for analytic and theoretical models to capture correctly, so it is encouraging to see it replicated so well by the LES. The inflection of the growth-rate curve is also captured well by the LES as the rarefaction portion of the BW has been observed to stop interacting with the interface at approximately 3 ms. This is evident in Fig. 15(a), as the 3 ms point marks the inflection point of the mixed-width growth rate.

Due to the combined nature of the instability (RMI followed by RTI), the growth rate illustrates elements of both instabilities' traditional behavior. While similar to RMI in that a finite amount of vorticity is deposited during BW interaction, the addition of RTI prolongs that deposition duration. The signature of the RTI is seen in the growth rate of the mixing layer, where a prolonged, nearly linear, increase in mixing rate is observed during early times. This is expected as the instantaneous RMI serves to essentially pass the RTI an interface that is already growing into the nonlinear regime. This should lead to enhanced mixing as compared to traditional RMI flows, which is certainly observed here. However, the divergent nature of the geometry should have an opposite effect. That is, the movement of the interface up into regions of the chamber with more space should serve to decrease the mixed-width growth as the interface is forced to spread laterally. Finally, there are contributions to the mixing growth due to the prolonged compressibility of the flow field, caused

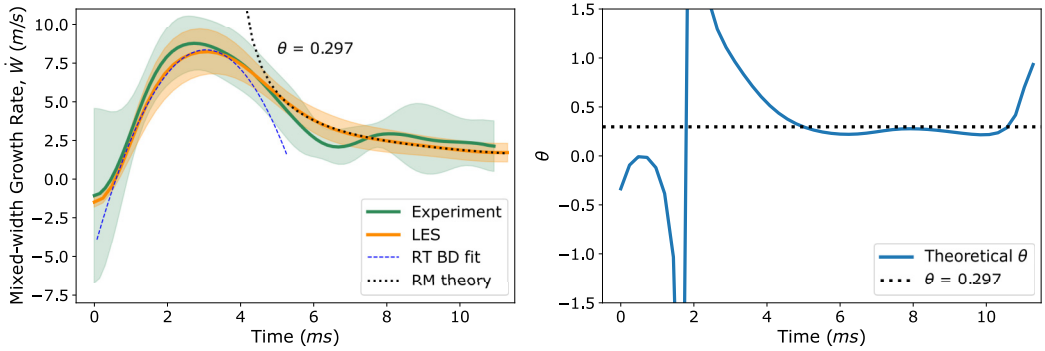


FIG. 15. 3D LES model: (Left) The ensemble comparison of the growth rate of W for the second IC characterization method. The mean of the ensemble is shown as the bold line, while the spread of results in each ensemble is represented by the shaded region which indicates \pm one standard deviation from the mean. Both the experimental and LES data are identically low-pass filtered prior to numerical differentiation. The linear+quadratic and power-law fits shown as dashed/dotted lines are applied to the LES data. (Right) The temporal development of θ (using LES data) according to Eq. 31 (Theoretical θ) compared to the value found from the power-law fit.

by the sustained interaction of the rarefaction portion of the BW and the interface. Considering all these complications present in the BDI, it is impressive that the LES is able to so closely track its mixing growth. The LES model can be said to capture the large-scale and fundamental physics of the problem and can be more confidently used in future problems like this.

Interestingly, Fig. 15(a) clearly shows three regimes of different growth-rate behavior: (1) RTI fueled growth-rate increase, (2) growth-rate inflection from increasing to decreasing, and (3) RMI like growth-rate decay. In the first regime at early times, the growth rate increases linearly. Linear growth-rate increases are predicted by self-similar RTI theory [derivative of Eq. (26)]; however, this is likely not applicable in the current scenario. First, it is certainly not in the self-similar growth regime, as the early images of the BDI show (Figs. 10 and 13). Further, this regime of the BDI is exceptionally dynamic due to the transition from a linear to nonlinear instability, large divergence effects as the interface moves up the chamber, rapid order-of-magnitude decreases in the deceleration magnitude caused by the BW, and peak compressibility effects due to the passing rarefaction. None of these complications were taken into account in the derivation of Eq. (26). Indeed, for all the complications mentioned (divergence, compressibility, transitioning, large deceleration) it is unreasonable to expect that any theoretical estimate of RTI growth (linear or nonlinear) will be able correctly predict BDI behavior in this regime. This highlights the necessity of using validated simulations to gain a better understanding in this regime.

However, an attempt to create an ad hoc fit originating from first principles may still be informative. If one instead assumes the mixed width is governed by a balance of buoyancy and drag forces as has been done for many previous RTI flows [72–74], then a more applicable form of an equation fit may be obtained. By starting with these classic buoyancy drag equations, neglecting the drag term (due to large deceleration in the regime of interest), linearizing the deceleration $g(t)$ such that

$$g(t) \approx g_o + \frac{dg_o}{dt}t, \quad (29)$$

and then integrating leads to

$$\dot{W} = C_1 A g_o t + \frac{1}{2} A \frac{dg_o}{dt} t^2 C_2 + \dot{W}_o. \quad (30)$$

Here g_o is the mean deceleration over the first millisecond, and $\frac{dg_o}{dt}$ is the mean deceleration rate over that same time. The constants C_1 and C_2 are fitting parameters and \dot{W}_o can be estimated using linear RMI theory: $\dot{W}_o = W_o A k \Delta V$ [3]. This fit (“RT BD fit”) is applied to the LES data in the first and second regime, and one can see it captures the behavior well in Fig. 15(a). The linearization of the driving deceleration allows for the combination of a linear and quadratic fit, which appears to match the flow behavior. While by no means a predictive model, it could perhaps serve as a step in that direction.

In the second regime, once the BW has stopped interacting with the interface, vorticity deposition should cease and the growth rate should transition from increasing to decreasing. This regime is governed by neither traditional RMI or RTI and is likely distinct to the BDI.

Once the growth-rate peaks and begins to decrease, the BDI enters the third regime. In this regime, one expects the growth rate to decay according to traditional RMI theory (due to the *finite* deposition of vorticity in both RMI and BDI). This decay can be expressed as $\dot{W} = B \theta (t - t_o)^{\theta-1}$, where B is a dimensional fitting constant and t_o is the time at which the BW stops interacting with the interface [58]. A power-law according to this equation is fit to the LES data in Fig. 15(a), and the best-fit value for θ is shown on the plot. Observing this relationship, one can see that RMI theory seeks the behavior of decaying, anisotropic, and homogeneous turbulence. This is certainly applicable for the BDI mixing layer during midlate times (Figs. 10 and 13) where the RMI fit is applied. One can also get an idea of how the RMI decay exponent, θ , changes in time by following methods used in Thornber *et al.* [58]. Namely, a time varying θ value is estimated using

$$\theta^{-1} = (1 - \ddot{W} W / \dot{W}^2). \quad (31)$$

Applying this relationship to the LES data results in the temporal θ behavior shown in Fig. 15(b). The horizontal dashed line indicates the θ value found using the power-law fit, which is seen to agree quite well with the asymptotic value predicted by Eq. (31). The spikes seen at early-mid times are due to the BDI behavior in the first and second regimes, where Eq. (31) obviously does not apply. The midlate time behavior displayed in Fig. 15(b) further indicates that the BDI decays very similarly to the RMI. Indeed the θ values found using the power-law and Eq. (31) fall within the range reported in literature [11,58].

VIII. CONCLUSION

This article presented a hierarchical validation scheme that used ensembles of experimental data to compare QOIs with three different models. First, a 2D Euler model was used to recreate the experimental facility and its driving physics. Boundary and initial conditions were successfully modeled and a drag-based loss model was added to account for unmeasured losses in the experimental facility. GP optimization showed the tuned Euler model was relatively insensitive to changes in model parameters.

The validated Euler model was then used as a basis for the implementation of a 2D RANS and 3D LES model, which were validated against ensembles of mixing data from separate experimental campaigns. It was necessary to use three model parameters for optimizing the RANS model, which showed good agreement in mixing statistics once the flow approached turbulence. The optimized model also showed that the rate of energy dissipation in the RANS model matched that of the experiment, despite large differences in TKE magnitude. However, the agreement in energy dissipation rate was only achieved after allowing for tuning of θ . Overall the RANS model displayed more limited predictive capability compared to the LES model. More work, beyond the scope of this paper, is needed to rigorously tune and validate this K - L RANS model to increase its appropriateness for use in transitioning flows such as this.

To validate the LES model, we generated a simulation ensemble of equal size to the experimental data ensemble. This allowed for the comparison of mean and variance trends for the mixing QOI. While, the validated LES model had no model parameters to optimize it was shown to be sensitive to the method used for the characterization of ICs. Directly inputting experimental ICs into the LES

TABLE III. Definitions and nomenclature appearing in this work.

BC	Boundary condition
BW	Blast wave
DCT	Discrete cosine transform
DPT	Dynamic pressure transducer
GP	Gaussian process
IC	Initial condition
ICF	Inertial confinement fusion
KHI/KH	Kelvin-Helmholtz instability
LES	Large-eddy simulation
LLNL	Lawrence Livermore National Lab
PIV	Particle image velocimetry
QOI	Quantities of interest
RANS	Reynolds averaged Navier Stokes
RMI/RM	Richtmyer-Meshkov instability
RP80	Detonator with 0.2 g high explosive
RTI/RT	Rayleigh-Taylor instability
SN	Supernova
TKE	Turbulent kinetic energy
A	Atwood number $\frac{\rho_h - \rho_l}{\rho_h + \rho_l}$
a	1/2 Peak-to-valley amplitude or mixed width
C_o	Euler model drag coefficient
E_o	Euler model initial pill energy
\dot{a}	Mixed-width growth rate
$g(t)$	Interface acceleration
Γ	Model-dependent source/sink terms
K	RANS model turbulent kinetic energy
k	Experimental estimate of turbulent kinetic energy
κ	Wave number
L	RANS model turbulent length scale
λ	Wavelength
M	Mach number
Re	Reynolds number
θ	RM self-similar growth exponent
W	Integral mixed width
Y_H	Heavy gas mass fraction

model led to much better overall agreement between the data ensembles for both mixing width and its growth rate. The LES model was shown to capture all of the relevant physics present in the BDI experiments. The LES also helped to elucidate information about the three mixing regimes observed in the BDI. Both similarities and differences with traditional RTI and RMI were observed. Primarily, the BDI was shown to decay according to RMI theory at late times.

Further work with these data sets can be pursued by investigating further comparison between LES and RANS simulations for QOIs that are not available experimentally. This could also help inform more general comparison between the RANS and LES models themselves, beyond just the QOI outputs. Additionally, a more formal uncertainty quantification of model parameters could be completed. For example, acquiring distributions of parameter uncertainty as opposed to just means. Further, much more work can be done to elucidate the complex behavior of the first mixing regime. Validated simulations can be compared to a range of linear and nonlinear theories, or analytical models, that have been developed to address different complications in the traditional RTI.

The resulting validated digital twin can be used in numerous direction for future work. It can be used to inform design modifications to the experimental facility, or for experimental campaign

planning when expanding the tested parameter space. The parameter space of BW strength and Atwood number can be further, and more easily, investigated using the validated RANS and LES models to investigate different BDI regimes. Further the results of these investigations could allow for the creation of GPs that replicate the RANS and LES models themselves. This would allow for a much more computationally efficient investigation of very large areas in the parameter space of the BDI.

ACKNOWLEDGMENTS

The authors thank Dr. Brandon Morgan for his consultation on using RANSbox and for his invaluable insight concerning the interpretation of RANS results. Thanks are also in order for Erin Wilson regarding her immense contributions to the aesthetic of plots and figures in this article. The authors also thank Ben's van, which facilitated much of this work. The first author is also incredibly thankful for the funding and opportunities provided by the DOE NNSA Stewardship Science Graduate Fellowship (SSGF) and the LLNL Defense Science and Technology Fellowship (DSTI). In addition, we acknowledge support from the DOE Early Career Award and Office of Fusion Energy Science in the form of Grant No. DE-SC0016181. Finally, this work was performed under the auspices of the U.S. Department of Energy by Lawrence Livermore National Laboratory under Contract No. DE-AC52-07NA27344.

-
- [1] W. D. Arnett, J. N. Bahcall, R. P. Kirshner, and S. E. Woosley, Supernova 1987A, *Annu. Rev. Astron. Astrophys.* **27**, 629 (1989).
 - [2] E. Mueller, B. Fryxell, and D. Arnett, Instability and clumping in SN 1987A, *Astron. Astrophys.* **251**, 505 (1991).
 - [3] R. D. Richtmyer, Taylor instability in shock acceleration of compressible fluids, *Commun. Pure Appl. Math.* **13**, 297 (1960).
 - [4] E. E. Meshkov, Instability of the interface of two gases accelerated by a shock wave, *Fluid Dyn.* **4**, 101 (1969).
 - [5] L. Rayleigh, Investigation of the character of the equilibrium of an incompressible heavy fluid of variable density, *Proc. London Math. Soc.* **s1-14**, 170 (1883).
 - [6] G. Taylor, The instability of liquid surfaces when accelerated in a direction perpendicular to their planes. I, *Proc. R. Soc. London A* **201**, 192 (1950).
 - [7] L. I. Sedov, *Similarity and Dimensional Methods in Mechanics* (CRC Press, Boca Raton, FL, 1993).
 - [8] C. E. Needham, *Shock Wave and High Pressure Phenomena Shock Wave and High Pressure Phenomena* (Springer, Berlin, 2010).
 - [9] A. R. Miles, Bubble merger model for the nonlinear Rayleigh-Taylor instability driven by a strong blast wave, *Phys. Plasmas* **11**, 5140 (2004).
 - [10] Y. Zhou, Rayleigh-Taylor and Richtmyer-Meshkov instability induced flow, turbulence, and mixing. I, *Phys. Rep.* **720–722**, 1 (2017).
 - [11] Y. Zhou, Rayleigh-Taylor and Richtmyer-Meshkov instability induced flow, turbulence, and mixing II, *Phys. Rep.* **723–725**, 1 (2017).
 - [12] V. Rana, H. Lim, J. Melvin, J. Glimm, B. Cheng, and D. H. Sharp, Mixing with applications to inertial-confinement-fusion implosions, *Phys. Rev. E* **95**, 013203 (2017).
 - [13] V. N. Goncharov, P. McKenty, S. Skupsky, R. Betti, R. L. McCrory, and C. Cherfils-Cl  rouin, Modeling hydrodynamic instabilities in inertial confinement fusion targets, *Phys. Plasmas* **7**, 5118 (2000).
 - [14] A. R. Miles, D. G. Braun, M. J. Edwards, H. F. Robey, R. P. Drake, and D. R. Leibrandt, Numerical simulation of supernova-relevant laser-driven hydro experiments on OMEGA, *Phys. Plasmas* **11**, 3631 (2004).
 - [15] O. A. Hurricane, D. A. Callahan, D. T. Casey, P. M. Celliers, C. Cerjan, E. L. Dewald, T. R. Dittrich, T. D  ppner, D. E. Hinkel, L. F. Hopkins, J. L. Kline, S. Le Pape, T. Ma, A. G. Macphée, J. L. Milovich,

- A. Pak, H. S. Park, P. K. Patel, B. A. Remington, J. D. Salmonson *et al.*, Fuel gain exceeding unity in an inertially confined fusion implosion, *Nature* **506**, 343 (2014).
- [16] N. B. Meezan, M. J. Edwards, O. A. Hurricane, P. K. Patel, D. A. Callahan, W. W. Hsing, R. P. Town, F. Albert, P. A. Amendt, L. F. Berzak Hopkins, D. K. Bradley, D. T. Casey, D. S. Clark, E. L. Dewald, T. R. Dittrich, L. Divol, T. Döppner, J. E. Field, S. W. Haan, G. N. Hall *et al.*, Indirect drive ignition at the National Ignition Facility, *Plasma Phys. Controlled Fusion* **59**, 014021 (2017).
- [17] T. Ma, P. K. Patel, N. Izumi, P. T. Springer, M. H. Key, L. J. Atherton, L. R. Benedetti, D. K. Bradley, D. A. Callahan, P. M. Celliers, C. J. Cerjan, D. S. Clark, E. L. Dewald, S. N. Dixit, T. Döppner, D. H. Edgell, R. Epstein, S. Glenn, G. Grim, S. W. Haan *et al.*, Onset of Hydrodynamic Mix in High-Velocity, Highly Compressed Inertial Confinement Fusion Implosions, *Phys. Rev. Lett.* **111**, 085004 (2013).
- [18] X. Ribeyre, V. T. Tikhonchuk, and S. Bouquet, Compressible Rayleigh-Taylor instabilities in supernova remnants, *Phys. Fluids* **16**, 4661 (2004).
- [19] Y. Zhou, T. T. Clark, D. S. Clark, S. Gail Glendinning, M. Aaron Skinner, C. M. Huntington, O. A. Hurricane, A. M. Dimits, and B. A. Remington, Turbulent mixing and transition criteria of flows induced by hydrodynamic instabilities, *Phys. Plasmas* **26**, 080901 (2019).
- [20] O. L. Landen, K. L. Baker, D. S. Clark, V. N. Goncharov, B. A. Hammel, D. D. Ho, O. A. Hurricane, J. D. Lindl, E. N. Loomis, L. Masse, C. Mauche, J. L. Milovich, J. L. Peterson, V. A. Smalyuk, S. A. Yi, A. L. Velikovich, and C. Weber, Indirect-drive ablative Richtmyer-Meshkov mode scaling, in *Journal of Physics: Conference Series* (Institute of Physics Publishing, Bristol, UK, 2016), Vol. 717, p. 012034.
- [21] E. Johnsen, J. Larsson, A. V. Bhagatwala, W. H. Cabot, P. Moin, B. J. Olson, P. S. Rawat, S. K. Shankar, B. Sjogreen, H. Yee, X. Zhong, and S. K. Lele, Assessment of high-resolution methods for numerical simulations of compressible turbulence with shock waves, *J. Comput. Phys.* **229**, 1213 (2010).
- [22] M. Vandenboomgaerde, P. Rouzier, D. Souffland, L. Biamino, G. Jourdan, L. Houas, and C. Mariani, Nonlinear growth of the converging Richtmyer-Meshkov instability in a conventional shock tube, *Phys. Rev. Fluids* **3**, 014001 (2018).
- [23] L. F. Wang, J. F. Wu, W. H. Ye, W. Y. Zhang, and X. T. He, Weakly nonlinear incompressible Rayleigh-Taylor instability growth at cylindrically convergent interfaces, *Phys. Plasmas* **20**, 042708 (2013).
- [24] X. Luo, F. Zhang, J. Ding, T. Si, J. Yang, Z. Zhai, and C. Y. Wen, Long-term effect of Rayleigh-Taylor stabilization on converging Richtmyer-Meshkov instability, *J. Fluid Mech.* **849**, 231 (2018).
- [25] M. Li, J. Ding, Z. Zhai, T. Si, N. Liu, S. Huang, and X. Luo, On divergent Richtmyer-Meshkov instability of a light/heavy interface, *J. Fluid Mech.* **901**, A38 (2020).
- [26] B. J. Olson, J. Larsson, S. K. Lele, and A. W. Cook, Nonlinear effects in the combined Rayleigh-Taylor/Kelvin-Helmholtz instability, *Phys. Fluids* **23**, 114107 (2011).
- [27] N. J. Mueschke and O. Schilling, Investigation of Rayleigh-Taylor turbulence and mixing using direct numerical simulation with experimentally measured initial conditions. I. Comparison to experimental data, *Phys. Fluids* **21**, 014106 (2009).
- [28] I. Boureima, P. Ramaprabhu, and N. Attal, Properties of the turbulent mixing layer in a spherical implosion, *J. Fluids Eng.* **140**, 050905 (2018).
- [29] M. Mohaghar, J. Carter, B. Musci, D. Reilly, J. McFarland, and D. Ranjan, Evaluation of turbulent mixing transition in a shock-driven variable-density flow, *J. Fluid Mech.* **831**, 779 (2017).
- [30] B. Thornber, D. Drikakis, D. L. Youngs, and R. J. Williams, The influence of initial conditions on turbulent mixing due to Richtmyer-Meshkov instability, *J. Fluid Mech.* **654**, 99 (2010).
- [31] W. K. George and L. Davidson, Role of initial conditions in establishing asymptotic flow behavior, *AIAA J.* **42**, 438 (2004).
- [32] G. Dimonte, Nonlinear evolution of the Rayleigh-Taylor and Richtmyer-Meshkov instabilities, *Phys. Plasmas* **6**, 2009 (1999).
- [33] B. J. Balakumar, G. C. Orlicz, J. R. Ristorcelli, S. Balasubramanian, K. P. Prestridge, and C. D. Tomkins, Turbulent mixing in a Richtmyer-Meshkov fluid layer after reshock: Velocity and density statistics, *J. Fluid Mech.* **696**, 67 (2012).
- [34] K. Kadau, C. Rosenblatt, J. L. Barber, T. C. Germann, Z. Huang, P. Carle, and B. J. Alder, The importance of fluctuations in fluid mixing, *Proc. Natl. Acad. Sci. USA* **104**, 7741 (2007).

- [35] P. Ramaprabhu, G. Dimonte, and M. J. Andrews, A numerical study of the influence of initial perturbations on the turbulent Rayleigh-Taylor instability, *J. Fluid Mech.* **536**, 285 (2005).
- [36] A. Banerjee and M. J. Andrews, 3D simulations to investigate initial condition effects on the growth of Rayleigh-Taylor mixing, *Int. J. Heat Mass Transf.* **52**, 3906 (2009).
- [37] D. L. Youngs, The density ratio dependence of self-similar Rayleigh-Taylor mixing, *Philos. Trans. R. Soc. A* **371**, 20120173 (2013).
- [38] C. Barmarousis and D. Drikakis, Multidimensional quantification of uncertainty and application to a turbulent mixing model, *Int. J. Numer. Methods Fluids* **85**, 385 (2017).
- [39] T. T. Clark and Y. Zhou, Self-similarity of two flows induced by instabilities, *Phys. Rev. E* **68**, 066305 (2003).
- [40] Q. Zhou, Temporal evolution and scaling of mixing in two-dimensional Rayleigh-Taylor turbulence, *Phys. Fluids* **25**, 085107 (2013).
- [41] K. Narayanan and R. Samtaney, Appearance of deterministic mixing behavior from ensembles of fluctuating hydrodynamics simulations of the Richtmyer-Meshkov instability, *Phys. Rev. E* **97**, 043111 (2018).
- [42] S. B. Dalziel, P. F. Linden, and D. L. Youngs, Self-similarity and internal structure of turbulence induced by Rayleigh-Taylor instability, *J. Fluid Mech.* **399**, 1 (1999).
- [43] G. Dimonte and R. Tipton, K-L turbulence model for the self-similar growth of the Rayleigh-Taylor and Richtmyer-Meshkov instabilities, *Phys. Fluids* **18**, 085101 (2006).
- [44] B. E. Morgan and J. A. Greenough, Large-eddy and unsteady RANS simulations of a shock-accelerated heavy gas cylinder, *Shock Waves* **26**, 355 (2016).
- [45] B. E. Morgan, M. O. Osawe, and M. S. Ulitsky, *RANSBox Users Guide. Version 0.3*, Tech. Rep. (Lawrence Livermore National Laboratory, Livermore, CA, 2022).
- [46] <https://github.com/LLNL/pyranda>.
- [47] B. Musci, S. Petter, G. Pathikonda, B. Ochs, and D. Ranjan, Supernova hydrodynamics: A lab-scale study of the blast-driven instability using high-speed diagnostics, *Astrophys. J.* **896**, 92 (2020).
- [48] J. Grun, J. Stamper, C. Manka, J. Resnick, R. Burris, J. Crawford, and B. H. Ripin, Instability of Taylor-Sedov Blast Waves Propagating Through a Uniform Gas, *Phys. Rev. Lett.* **66**, 2738 (1991).
- [49] J. J. MacFarlane, G. A. Moses, and R. R. Peterson, Energy deposition and shock wave evolution from laser-generated plasma expansions, *Phys. Fluids B* **1**, 635 (1989).
- [50] A. W. Cook, Artificial fluid properties for large-eddy simulation of compressible turbulent mixing, *Phys. Fluids* **19**, 055103 (2007).
- [51] B. E. Morgan, B. J. Olson, W. J. Black, and J. A. McFarland, Large-eddy simulation and Reynolds-averaged Navier-Stokes modeling of a reacting Rayleigh-Taylor mixing layer in a spherical geometry, *Phys. Rev. E* **98**, 033111 (2018).
- [52] P. Kundu, I. Cohen, and D. Dowling, *Fluid Mechanics*, 6th ed. (Academic Press, San Diego, CA, 2015).
- [53] R. L. Panton, *Incompressible Flow* (John Wiley and Sons, New York, NY, 2013).
- [54] H. Blasius, *Boundary Layers in Liquids with Low Friction* (BG Teubner, Berlin, 1907).
- [55] H. Schlichting and K. Gersten, *Boundary-Layer Theory*, 9th ed. (McGraw-Hill, New York, NY, 2015), pp. 1–799.
- [56] B. E. Morgan, O. Schilling, and T. A. Hartland, Two-length-scale turbulence model for self-similar buoyancy-, shock-, and shear-driven mixing, *Phys. Rev. E* **97**, 013104 (2018).
- [57] T. T. Clark and Y. Zhou, Growth rate exponents of Richtmyer-Meshkov mixing layers, *J. Appl. Mech., Trans. ASME* **73**, 461 (2006).
- [58] B. Thornber, J. Griffond, O. Poujade, N. Attal, H. Varshochi, P. Bigdelou, P. Ramaprabhu, B. Olson, J. Greenough, Y. Zhou, O. Schilling, K. A. Garside, R. J. Williams, C. A. Batha, P. A. Kuchugov, M. E. Ladonkina, V. F. Tishkin, N. V. Zmitrenko, V. B. Rozanov, and D. L. Youngs, Late-time growth rate, mixing, and anisotropy in the multimode narrowband Richtmyer-Meshkov instability: The θ -group collaboration, *Phys. Fluids* **29**, 105107 (2017).
- [59] G. Dimonte and M. Schneider, Density ratio dependence of Rayleigh-Taylor mixing for sustained and impulsive acceleration histories, *Phys. Fluids* **12**, 304 (2000).
- [60] D. H. Sharp, An overview of Rayleigh-Taylor instability, *Physica D* **12**, 3 (1984).

- [61] A. W. Cook, W. Cabot, and P. L. Miller, The mixing transition in Rayleigh-Taylor instability, *J. Fluid Mech.* **511**, 333 (2004).
- [62] J. Glimm, J. W. Grove, X. L. Li, W. Oh, and D. H. Sharp, A Critical Analysis of Rayleigh-Taylor Growth Rates, *J. Comput. Phys.* **169**, 652 (2001).
- [63] J. W. Jacobs and S. B. Dalziel, Rayleigh-Taylor instability in complex stratifications, *J. Fluid Mech.* **542**, 251 (2005).
- [64] G. Dimonte, D. L. Youngs, A. Dimits, S. Weber, M. Marinak, S. Wunsch, C. Garasi, A. Robinson, M. J. Andrews, P. Ramaprabhu, A. C. Calder, B. Fryxell, J. Biello, L. Dursi, P. MacNeice, K. Olson, P. Ricker, R. Rosner, F. Timmes, H. Tufo, et al., A comparative study of the turbulent Rayleigh-Taylor instability using high-resolution three-dimensional numerical simulations: The Alpha-Group collaboration, *Phys. Fluids* **16**, 1668 (2004).
- [65] W. H. Cabot and A. W. Cook, Reynolds number effects on Rayleigh-Taylor instability with possible implications for type-Ia supernovae, *Nat. Phys.* **2**, 562 (2006).
- [66] B. J. Olson and A. W. Cook, Rayleigh-Taylor shock waves, *Phys. Fluids* **19**, 128108 (2007).
- [67] B. E. Morgan and M. E. Wickett, Three-equation model for the self-similar growth of Rayleigh-Taylor and Richtmyer-Meshkov instabilities, *Phys. Rev. E* **91**, 043002 (2015).
- [68] C. Weber, N. Haehn, J. Oakley, D. Rothamer, and R. Bonazza, Turbulent mixing measurements in the Richtmyer-Meshkov instability, *Phys. Fluids* **24**, 074105 (2012).
- [69] E. G. Sewell, K. J. Ferguson, V. V. Krivets, J. W. Jacobs, E. G. Sewell, K. J. Ferguson, V. V. Krivets, and J. W. Jacobs, Time-resolved particle image velocimetry measurements of the turbulent Richtmyer-Meshkov instability, *J. Fluid Mech.* **917**, A41 (2021).
- [70] M. Groom and B. Thornber, The influence of initial perturbation power spectra on the growth of a turbulent mixing layer induced by Richtmyer-Meshkov instability, *Physica D* **407**, 132463 (2020).
- [71] See Supplemental Material at <http://link.aps.org/supplemental/10.1103/PhysRevFluids.8.014501> for supplementary videos.
- [72] D. Oron, L. Arazi, D. Kartoon, A. Rikanati, U. Alon, and D. Shvarts, Dimensionality dependence of the Rayleigh-Taylor and Richtmyer-Meshkov instability late-time scaling laws, *Phys. Plasmas* **8**, 2883 (2001).
- [73] D. Layzer, On the instability of superposed fluids in a gravitational field, *Astrophys. J.* **122**, 1 (1955).
- [74] B. J. Grea, The rapid acceleration model and the growth rate of a turbulent mixing zone induced by Rayleigh-Taylor instability, *Phys. Fluids* **25**, 015118 (2013).